QUANTITATIVE MAGNETIC CHARACTERIZATION OF SINGLE CELLS

A DISSERTATION
SUBMITTED TO THE DEPARTMENT OF APPLIED PHYSICS
AND THE COMMITTEE ON GRADUATE STUDIES
OF STANFORD UNIVERSITY
IN PARTIAL FULFILLMENT OF THE REQUIREMENTS
FOR THE DEGREE OF
DOCTOR OF PHILOSOPHY

Lisa Qian
August 2013

This dissertation is online at: http://purl.stanford.edu/np251vz9144

I certify that I have read this dissertation and that, in my opinion, it is fully adequate in scope and quality as a dissertation for the degree of Doctor of Philosophy.

Kathryn Moler, Primary Adviser

I certify that I have read this dissertation and that, in my opinion, it is fully adequate in scope and quality as a dissertation for the degree of Doctor of Philosophy.

Malcolm Beasley

I certify that I have read this dissertation and that, in my opinion, it is fully adequate in scope and quality as a dissertation for the degree of Doctor of Philosophy.

Ian Fisher

Approved for the Stanford University Committee on Graduate Studies.

Patricia J. Gumport, Vice Provost for Graduate Education

This signature page was generated electronically upon submission of this dissertation in electronic format. An original signed hard copy of the signature page is on file in University Archives.

Abstract

Iron oxide based magnetic nanoparticles are used in a variety of biomedical applications, such as targeted drug delivery, cancer therapy and MRI. Superparamagnetic iron oxide (SPIO) particles are commonly used to enhance image contrast in MRI. However, traditional ways of labeling cells suffer from several drawbacks. For instance, false positives from dead cells are common, and MR signal can dilute as cells divide. A genetically encoded contrast agent would circumvent these problems, allowing for a persistent form of targeted MRI contrast. An effort described in this thesis seeks to express genes from magnetotactic bacteria, which naturally uptake iron to form iron oxide particles, in mammalian cancer cells.

In addition to developing new contrast agents, improvements in MR technology has made it possible to image individual cells [17]. This offers the potential to label and track individual stem cells or cancer cells using MRI. However in order to optimize pulse sequences for single cell imaging, it is necessary to develop magnetic characterization techniques capable of measuring the magnetic dipole moment of single cells. Traditional bulk magnetic characterization techniques measure properties of a large number of cells, but are insensitive to individual variations. To study single cells requires better magnetic sensitivity and spatial resolution.

In this thesis, I will give an overview of various characterization techniques and how they might be employed in various biological applications. We used scanning SQUID magnetometry to image the magnetic flux of individual magnetotactic bacteria and SPIO labeled mammalian cells and calculated the magnetic moment of each cell from these flux images. Because the instrument is typically used to study condensed matter samples, we developed new protocols for measuring biological cells.

By measuring many individual cells, we can compare our results with bulk magnetometry measurements to gain additional insights. We showed that while two different types of iron supplementation produce magnetotactic bacteria with different average magnetic moment per cell when measured in bulk, this is an effect dominated by a small number of cells. If we were to randomly sample individual cells from both populations, there would be no way of determining which group they originated from by measuring their magnetic moment.

Such single cell magnetic measurements will be helpful for optimizing image contrast in single cell MR tracking and other single cell applications.

Acknowledgements

My time in the Applied Physics department has been an amazing and educational experience in every way. I joined Professor Moler's lab my second quarter at Stanford. During my five and a half years in the lab, I have had many struggles and frustrations. Throughout it all, Kam has consistently been supportive and fair, allowing to grow as a scientist and as a person. Instead of telling me specifically what to do and how to do it, she allowed me to follow my own interests. This eventually led me to measure biological cells, which is something I would not have dreamed of studying when I first came to graduate school. I am so appreciative of Kam for her support and faith in me.

I am also fortunate to have had the opportunity to work with amazing collaborators from a wide array of backgrounds. Beena Kalisky has guided me every step of the way through this project, and I look up to her as a role model in many different ways. Bo Dwyer has worked on this project with me from the very beginning, when he was just a freshman, and has been consistently involved until he graduated this spring. John Kirtley is an amazingly talented scientist as well as a wonderful mentor. Outside of the Moler lab, I have been lucky enough to interact with various groups from the medical school. Mike Benoit and Professor AC Matin first came to us with the idea of measuring magnetotactic bacteria. Amanda Hamilton has provided all of our bacterial samples, and continued to provide us with samples as we transitioned to working with mammalian cells. Professor Brian Rutt has led the CIRM project, where I had the opportunity to work closely with Sui Seng Tee and others involved in the project. Working as a part of a multidisciplinary collaboration has allowed me to communicate and work with talented people from backgrounds very different

from, yet complementary to, mine. I have learned so much from interactions with my collaborators.

I'm also very fortunate to have been a part of the Moler Lab family. Many thanks to Cliff Hicks, Julie Bert, Nick Koshnick, Ophir Auslaender, Lan Luan, Beena Kalisky, Tom Lippman, Ilya Sochnikov, Katja Nowack, Eric Spanton, Hilary Noad, Bo Dwyer, Philip Kratz, Jenny Arps, and others for helping me through these six years.

The advice and support I've received from the staff at SNC (Stanford Nano Center), SNF (Stanford Nanofabrication) and SNL (Stanford Nanocharacterization Lab) have been invaluable. Tobi Beetz, Rich Tiberio, Rich Chin, Ann Marshall, Bob Jones, Chuck Hitzman and Jeff Tok have all been helped me on various instruments and microscopes. Thank you for your patience and kindness.

The Stanford Music Department has offered me incredible opportunities. After not playing for several years in college, never in my wildest dreams did I expect to take up music again and play with such talented people. In the past six years, I have toured China with the Stanford Symphony Orchestra and Van Cliburn piano competition winner Jon Nakamatsu, studied chamber music with the St. Lawrence String Quartet, played in a master class for the Julliard String Quartet, participated in a concerto competition, and played in chamber groups with professional musicians. Thank you Jindong Cai, Robin Sharp, the St. Lawrence String Quartet, and all my fellow musicians for these amazing experiences. I now know that I don't have to choose between being a scientist and a musician - both complement one another and define who I am.

Finally, I'd like to thank my family and friends. My father, Weida, came to the US in the late 1980's to pursue a PhD in Physics. Now, more than 20 years later, I am following in his footsteps. My parents have consistently been an inspiration to me, and have encouraged me in all of my endeavors. Finally, I am grateful to my wonderful boyfriend Matthias, without whom I would not be have completed this thesis. Thank you for always believing in me.

Contents

List of Tables

List of Figures

Chapter 1

Introduction

In this chapter, I will give an overview of how nanomagnets are used in medicine, particular for in-vivo magnetic resonance imaging (MRI). I'll also give a low-level background of MRI techniques and how the superparamagnetic properties of nanomagnets are used to enhance signal contrast in MRI. Finally, I will discuss various experimental techniques that can be used to study the magnetic properties of *single* nanomagnets, including the ones that have been used in this thesis work.

1.1 Iron oxide nanomagnets in medicine

Iron oxides are a collective term for particles with a crystalline core containing ferrous (Fe^{2+}) and or ferric (Fe^{3+}) ions and oxygen. Chemically synthesized iron oxide based nanomagnets can be used in a variety of biomedical applications. They are superparamagnetic, meaning that the magnetization of a collection of nanoparticles can be turned on and off by an external magnetic field.

Iron oxide nanoparticles are also known for their colloidal stability and relatively low cytotoxicity after being coated with hydrophilic and biocompatible substances, making them an ideal candidate for medical applications [31]. In addition, magnetic nanparticles have the potential to be multifunctional, meaning that once injected into a patient, they can serve a variety of purposes. Some applications include targeted drug delivery, local hyperthermia as a form of cancer therapy, gene therapy, tissue

engineering, and contrast agents for magnetic resonance imaging [20].

In this chapter, I will give a brief overview of the first four of these topics, and Section 1.2 will cover MRI in greater detail. The main challenge is to modify the shell surrounding the iron oxide core for a specific application. I will highlight some commonly used methods of synthesizing SPIO particles, and provide a few details about their magnetic properties.

1.1.1 Drug delivery

Nanoparticles offer significant opportunities for targeted treatment of diseases. Traditional nanocarrier drug delivery systems (DDS) cannot be monitored in vivo, meaning the biodistribution of the associated drugs cannot be monitored in real time. SPIOs are ideal agents for drug delivery systems because they are already widely used for MRI contrast agents.

Considerable research is still being conducted to make these nanomagnets function as both MRI contrast agents and drug delivery agents. A successful DDS needs to:

1. Successfully load the drug into the nanoparticle
2. Deliver the drug loaded nanoparticles to target cells
3. Preferentially bind nanoparticles to cancer cells over neighboring normal cells
4. Release the drugs to target cells in a controlled fashion
5. Allow for visualization of tumor cells before and after drug release
6. Remove nanoparticles from system when delivery is complete
7. All these steps must be completed without affecting healthy cells

The most common technique of load drugs into nanoparticles is to conjugate the drug of interest to be compatible with the particles' polymer shell. This allows the drug embedded into the polymer shell.

A main challenge of delivering the drug loaded particles is to prevent detection by the immune system. This can be achieved by carefully engineering the polymer

shell so that the resulting particle is water soluble and similar in size to a virus [15]. Such hydrophilic materials include dextran, polyethylene glycol, or block copolymers. However, recent work has shown that this effort may trigger the immune system in unexpected ways [42], and should be used with caution.

To ensure that the drugs are delivered properly, it is important that the magnetic nanoparticles bind preferentially to cancer cells and not to normal cells. This can be accomplished by functionalizing the nanoparticle surface with targeted ligands that bind to receptors or other molecules exclusive to malignant tumor cells. Some examples of targeting ligands include cell penetrating peptides (CPP) such as RGD-peptide and folic acid [31] [26].

Once the nanoparticles arrive at their target, they must release the drugs they are carrying in a controlled fashion. One approach is to design "smart" carriers that activate a targeting functional group in response to a stimulus. Such a stimulus needs to be unique to the tumor environment, but can be either intrinsic or extrinsic to the tumor cells. Examples include temperature, pH, or enzymatic cleavage induced stimuli [29]. For example, thermally responsive peptides and polymer nanoparticle coatings can be triggered to accumulate by an external application of local heat. This is an example of extrinsic triggering. The naturally acidic environment of malignant tumors can be used as an intrinsic stimulus. For instance, certain nanoparticle polymer coatings are capable of revealing targeting ligands in response to a pH level decrease from 7.2 to 6.8 [29].

1.1.2 Magnetic hyperthermia

Magnetic hyperthermia is an experimental cancer treatment, where magnetic nanoparticles are placed inside a tumor and an external AC magnetic field is used to raise the temperature of the tumor and damage or break it apart. Neel relaxation, Brownian motion and hysterisis loss are all contributing factors to the thermal energy release [4].

The AC magnetic field sweeps the magnetization vector of single domain particles back and forth, releasing the energy stored in the their hysterisis loops. The hysterisis of a single domain particle can be described using the Stoner-Wolhforth model of

magnetization reversal. The blocking temperature is dependent on the measurement time, or AC frequency [25].

In addition to Stoner-Wohlfarth switching, there is also magnetization reversal due to Brownian motion. Because the nanoparticles are suspended in a fluid (blood), they behave like a ferrofluid. An external AC magnetic field will cause the particles to rotate in the fluid, bringing its magnetization to align with the external field. A delay between this physical rotation and the field rotation causes hysterisis.

1.1.3 Gene therapy

Gene therapy refers to the use of genetic material (DNA/RNA) in specific cells or tissues to treat or prevent disease. This approach is a promising alternative to using drugs or surgery, and has shown promising results for treating hereditary diseases such as Parkinson's disease and Huntington's disease. Some of the approaches for gene therapy include: [31]

- Expressing heterogeneous genes into targeted cells
- Replacing mutated gene with a healthy copy of the gene
- "Knocking out", or deactivating, deleterious genes

The main limitation of gene therapy is the low transfection efficiencies of gene vectors, the DNA molecule that carries genetic information to the targeted cell. SPIO particles can be used to significantly improve the vector efficiency via a method called magnetic targeted transfection, or *magnetofection*. In this technique, vectors are associated with SPIO particles and an applied magnetic field is used to target gene delivery. Magnetofection has been shown to significantly improve vector accumulation and concentration at target tissues both *in vitro* and *in vivo* [39].

Magnetofection has the potential to lower the vector dose to target tissue as well as the incubation time required to achieve high transduction efficiency. Furthermore, it can be applied to any type of gene vector, although the size and surface chemistry of the SPIO particles may need to be adjusted [39].

1.1.4 Tissue engineering

Tissue engineering was developed in the early 1990's with the aim of creating functional tissues using cells and biomaterials [27]. The general strategy is to embed tissue cells within matrices made from collagen or synthetic polymers. These systems can be implanted and become incorporated into the body.

A significant challenge is to micropattern cells to create functional tissue architectures. Much recent progress has been made to address this concern, including surface chemistry, cell spraying, and 3D printing. Magnetic nanoparticles can be used for magnetic force assisted tissue engineering. For example, recent research has successfuly labeled cells with 10nm magnetite nanoparticles which were then spatially patterned onto a cell-adhesive surface using an external magnet [19].

1.2 Magnetic Resonance Imaging

Magnetic Resonance Imaging(MRI) is a commonly used diagnostic tool in medicine. It is non-invasive, uses non-ionizing radiation, and offers flexibility to customize imaging parameters different tissues. These reasons make it an ideal imaging and diagnostic tool for many medical applications.

MR techniques study the interactions between an external magnetic field and nuclear spin. Atoms with zero nuclear spin (such as ^{12}C or ^{16}O) do not interact with external magnetic fields and thus cannot be studied with MR. The hydrogen nucleus, ^{1}H, has spin 1/2 and a large magnetic susceptibility. It is also abundant in biological specimens, and is therefore a natural choice for imaging tissues using MR. Therefore, most MRI experiments visualize the ^{1}H nucleus.

An MR measurement works as follows. The sample (or a patient) is exposed to electromagnetic energy at a specific frequency. Excited nuclei reemit this energy as they relax, which is then recorded and processed to form an image. What this image shows is based on the interactions of nuclear spins within a sample with three types of magnetic fields: the static field B_0, a radiofrequency pulse field B_1, and linear gradient fields G.

1.2.1 Static field B_0

An individual ^{1}H nucleus has spin 1/2, and therefore a little magnetic dipole moment associated with it. In a zero field environment, however, a macroscopic collection of hydrogen atoms, such as a piece of tissue, do not have a net magnetic moment because under each of the nucleus spins are randomly oriented. When an external magnetic field, $\boldsymbol{B_0}$, is applied, the proton spins will precess about the axis parallel to $\boldsymbol{B_0}$ with the Larmor frequency:

$$\omega_0 = \frac{\gamma B_0}{2\pi} \tag{1.1}$$

Equation 1.1 describes the frequency of precession in Hz as a function of applied magnetic field strength B_0 in units of Tesla (T) and the gyromagnetic ratio γ in $\mathrm{s}^{-1}\mathrm{T}^{-1}$, which describes the ratio between a particle's magnetic dipole moment to its angular momentum.

By convention, the axis of precession and $\boldsymbol{B_0}$ is labeled as the z-axis. Because the precessing spins' phases are not synchronized, there is no net magnetization in the x-y plane perpendicular to $\boldsymbol{B_0}$ ($M_{xy} = 0$). In the z direction, more protons spins will align with $\boldsymbol{B_0}$ than against it, proportional to $e^{-\frac{\Delta E}{kT}}$. The Zeeman energy splitting between spin up and spin down protons, ΔE, is proportional to B_0.

$$\Delta E = h\omega_0 = \frac{h\gamma B_0}{2\pi} \tag{1.2}$$

This spin imbalance creates a net magnetic moment along the z-axis, M_z. Most whole body imaging systems operate at a fixed B_0 within the range of 0.1 to 3T. For most bodily tissues in this range, M_0 is proportional to B_0,. The constant of proportionality χ is known as the magnetic susceptibility.

$$\boldsymbol{M_0} = \chi \boldsymbol{B_0} \tag{1.3}$$

1.2.2 RF field, B_1

With just a static field, the protons spins are precessing along the z-axis at the Larmor frequency in an unsynchronized manner. $\boldsymbol{M_0}$ is aligned with $\boldsymbol{B_0}$, $M_{xy} = 0$, and the

proton spins are in an equilibrium state. To excite these spins, an AC radio frequencey (RF) magnetic pulse $\boldsymbol{B_1}$, on the order of a few Gauss, is applied in the transverse x-y plane. If the frequecy of this pulse is tuned to the the Larmor frequency ω_0, the spins will be excited out of equilibrium, causing the net magnetization $\boldsymbol{M}$ to rotate towards the x-y plane, perpendicular to both $\boldsymbol{B_0}$ and $\boldsymbol{B_1}$. If the pulse is sufficiently long and high in amplitude, $\boldsymbol{M}$ can be made to lie entirely on the transverse plane. Such a pulse is the so called $\pi/2$-pulse, or 90° pulse.

After the excitation pulse is turned off, the spins will relax back to equilibrium, emitting energy at ω_0 during the process. The protons precess in phase about $\boldsymbol{B_0}$. This coherently rotating magnetic field induces a current in an RF receiver coil placed perpendicular to the transverse plane. This induced signal is known as the *free electron decay* (FID) - this is the measured MR signal.

The frequency and phase of the FID signal with respect to the transmitted RF pulse, along with its amplitude decay rate, are tissue dependent. For instance, T_1, the time constant of M relaxing back to z-axis, ranges between 100-2000 ms depending on the tissue. T_2, the decay constant of the transverse component of M, ranges from 10-300 ms. Mapping out the spatial distribution of these parameters produces an MR image.

1.2.3 Relaxation

The process in which protons release energy after the RF pulse is known as relaxation. As described in section 1.2.2, T_1 is known as the longitudinal relaxation time and describes the time it takes for the longitudinal component of $\boldsymbol{M}$ to align back with the z axis:

$$M_z(\tau) = M_0(1 - e^{-\tau/T1}) \tag{1.4}$$

whtere τ is the time following the RF pulse. The T_1 relaxation time is also known as *spin-lattice* relaxation time becuase it is a measurement of the time it takes for the excited spins to give its energy back to the surrounding lattice, rather than to other protons.

The transverse relaxation time T_2 describes how quickly M_{xy} decays to zero. It is

also known as the *spin-spin* relaxation because it refers to how quickly spin dephasing occurs. At the moment the RF pulse is switched off, proton spins are in phase, precessing at frequency ω_0. Protons in close proximity to each other couple with each other since they are emitting and absorbing energy at the same frequency, ω_0. Vibrations and rotations cause the ω_0 of neighboring protons to fluctuate, resulting in decoherence. T_2 is usually 5-10 times shorter than T_1, and depends on the density of protons.

T_2 only describes decay in M_{xy} caused by spin-spin interactions. Magnetic inhomogeneities can also cause local perturbations in the Larmor frequency, causing spin dephasing to occur more rapidly. Non-uniformity in $\boldsymbol{B_0}$ can arise from imperfections in the main static field source and from inhomogeneities in sample susceptibility and/or magnetic polarization of adjacent tissues. These sources contribute to the total transverse relaxation time T_2^*:

$$M_{xy}(\tau) = M_{xy,max} e^{-\tau/T_2^*} \tag{1.5}$$

where $M_{xy,max}$ refers to the transverse magnetization immediately following the RF pulse. This decaying oscillation is the FID signal that is measured in an MR experiment.

T_2 can be separated from T_2^* by using a spin echo sequence. First, a 90° RF pulse is applied, rotating the magnetization entirely onto the transverse plane. After a time delay t, during which spin dephasing occurs with time constant T_2^*, a 180° RF pulse is applied. This "inversion" pulse reverses the phases of the proton spins, so that the spins that precessed faster due to stationary inhomogeneities are now trailing the net magnetization vector. After time t, the spins will regain coherence to produce the echo signal:

$$M_{xy}(\tau) = M_{xy,max} e^{-2\tau/T_2} \tag{1.6}$$

Spin-spin relaxation cannot be recovered using a π-pulse. However, for most applications, decoherence due to static inhomogeneities are dominant.

1.2.4 Image Constrast

Image contrast is a result of spatial differences in relaxation times of tissues. TE and TR can be chosen to accentuate these differences and increase contrast. To obtain three dimensional MR images, linear gradient fields $\boldsymbol{G}$ are superimposed onto the main background magnetic field $\boldsymbol{B_0}$. These gradient fields are small perturbations to $\boldsymbol{B}$, resulting in variations less than 1% of the total field. These variations change the local Larmor frequency of protons in the gradient field:

$$\omega(\boldsymbol{r_i}) = \gamma(B_0 + \boldsymbol{G} \cdot \boldsymbol{r_i}) \tag{1.7}$$

where $\omega(\boldsymbol{r_i})$ is the proton frequency at position r_i. Thus, protons within a specimen can be made to resonate at different frequencies depending on their positions within the gradient field, allowing for 3-dimensional imaging. An RF pulse will only excite a certain "slice" of tissue, normal to the direction of $\boldsymbol{G}$. Larger G gives thinner slices, but also less signal because there are fewer protons in each slice.

An MR image is a frequency and phase map of protons. Each pixel of the image represents volume elements (voxels) of tissue, whose intensity depends on the proton density of the voxel, weighted by their T_1 and T_2 relaxation times.

Pulse sequences

MR images are obtained by applying series of pulse sequences and detecting the FID signal in the presence of a readout gradient field $\boldsymbol{G_{RO}}$. As described in the previous section, measuring local relaxation times allow for natural contrast between some tissue types. The pulse sequence can be designed in such a way to enhance tissue contrast. The parameters to vary in a typical sequence are TE, the gradient echo time, and TR, the sequence repetition time. TR is the time between excitation pulses. In general, $TR >> T_2$, so that the transverse magnetization has completely decayed before another excitation pulse. By shortening TR so that it is slightly less than T1, M_z never reaches full magnetization between pulses. This enhances variations in T1 relaxation, or the T1 effect. (see figure)

TE is the short time period between the end of the RF pulse and measurement

time, which is used to introduce a T_2^* dependence. Combining the two, the signal intensity at location (x, y) of a slice is given by:

$$I(x,y) \propto \rho(x,y)(1 - e^{-\frac{TR}{T_1(x,y)}})e^{-\frac{TE}{T_2^*(x,y)}} \tag{1.8}$$

Longer TE gives better T2* contrast, but is limited by the dephasing time. A spin echo sequence can be ued to obtain longer TE for better T_2 discrimination. (see figure).

Here, a 180° pulse is applied time time TE/2 after the 90° pulse. We assume that $TE/2 \ll T_1$ so that the 180° pulse does not affect M_z. With a spin-echo pulse, the readout at time TE depends on T_2, not T_2^*.

Much work has been done to optimize TE and TR for appropriate tissue contrast. For example, water has a long T2 time because the polar bonds and low density make for slow dephasing time. Solids are the opposite, with short T2 times. Fats and proteins are intermediate. A T2 weighted sequency can be set up to accentuate these differences with a long TR to avoid T1 contrast, and TE$\approx T_2$.

T_1-weighted pulse sequences can be used to highlight differences in local Larmor frequencies. The Larmor frequency of hydrogen is 42.6MHz/Tesla, but the local value depends on the physical states of the tissue. For example, the polar bonds in water molecules cause the natural frequency to be much faster than that of pure hydrogen. Fats and proteins have ω_0 roughly equal to that of hydrogen. The energy transfer to the lattice is much more efficient in this case, so fats an proteins have a lower T_1 than water. A T_1-weighted pulse sequence, with short TE and TR$\approx T_1$ will accentuate this difference in the resulting image.

Frequency selective pulses

Another way of obtaining tissue contrast without introducing contrast agents is by looking at the frequency of the FID signal. The resonant frequency of protons can shift slightly due to magnetic shielding from the orbital motion of surrounding electrons, an effect known as *chemical shielding*. For example, water is a polar molecule comprised of two hydrogen atoms bonded to one oxygen atom, while fat molecule

are heterogeneous. Because of its electron polarization, a water proton experiences a slightly lower local magnetic field than does a non-polarized fat proton. This results in different resonance frequencies for water and fat protons under the same static field B_0. At 1.5T, the chemical shift is 220Hz, which is easily measureable. Such techniques are known as frequency selective saturation pulse sequences.

1.2.5 Contrast agents

Since it is a diagnostic tool, the goal of MRI is often to distinguish normal tissue from pathological, or disease tissue. Although the techniques described in Section 1.2.4 describe how to take advantage of intrinsic contrast between tissue types, it is often not enough. Pathological tissue could have the same relaxation times as normal tissue, or it could be embedded in normal tissue in small quantities, making signal from noise a problem. External contrast agents can be introduced to improve the SNR between pathological tissue and normal tissue.

Various intravenous contrast agents are available commercially. Typically, these agents are used to shorten the relaxation times of surrounding protons, shortening both T1 and T2. Agents that are used to decrease T1 relaxation time are gadolinium or manganese. These particles enhance the T1-weighted signals generated by surrounding protons. Since

$$I(x,y) \propto \rho(x,y)(1 - e^{-\frac{TR}{T_1(x,y)}})e^{-\frac{TE}{T_2^*(x,y)}} \tag{1.9}$$

lowering T1 increases the received signal, providing positive image contrast. In contrast, locally suppressing T2 relaxation times decreases the received signal and provides negative image contrast. Agents that shorten T2 relaxation times are superparamagnetic iron oxide (SPIO) particles. The large magnetic susceptibility of these particles alter the local magnetic field, prolonging the decoherence time of the protons in its vicinity.

SPIO particles are generally 4 to 10nm in diameter and its biological behavior can be altered by coatings. They are typically much more effective for T2 suppression than for T1 suppression, so there are used for reducing signal intensity of targeted

tissue on T2 weighted images (negative contrast).

Two types of SPIO particles discussed in this work are Molday ION™and Bangs BioMag® beads. Molday ION™is comprised of roughly 30nm iron oxide based particles, available for purchase through BioPhysics Assay Laboratory (BioPAL) Inc. It has a half-life in blood of several hours and is compatible in a wide range of vascular research. BioMag superparamagnetic particles from Bangs Labs are not FDA approved for use as intravenous contrast agents, but they are widely used for magnetic separation of cells and other types of molecules. They have a mean diameter of 1.5μm, much larger than the Molday ION™particles.

1.3 Magnetic characterization methods

In this section, I will provide an overview of different microscopy methods that exist currently for measuring magnetic properties of nano-scaled material - both in bulk and at the individual particle level.

Bulk magnetometers can be used to efficiently study the average properties of a collection of magnetic particles. However, they lack the sensitivity to study *individual* nanomagnets, which is the goal of this thesis.

Various techniques can be employed to measure magnetic signals from single magnetic nanoparticles. We can study the interaction between magnetism and electrons using electron microscopy techniques or the interaction between magnetism and photons using X-ray techniques. We can also use scanning SQUIDs to measure magnetometry and susceptometry, or magnetic force microscopy to spatially resolve magnetic forces.

The main goal of this thesis is to study the magnetic moments of individual magnetically labeled cells for potential use as single cell MR trackers. Thus, the ideal characterization instrument should have the following capabilities:

- Spatial resolution $\lesssim 1\mu$m
- Magnetic sensitivity $\lesssim 10^5 \mu_B$
- Ability to measure large number of particles in a single experiment (>100)

- Ability to measure close to room temperature (ideally at 37°)

1.3.1 Bulk Magnetometers

Bulk magnetometers tend to be generally straight forward to use with a quick turnaround, with usually large temperature ranges. However, their sensitivity is not high enough to measure individual cells. These instruments are ideal for looking at properties of a large ensemble of particles, for either initial assessment or for comparison to individual measurements.

In this thesis work, all bulk measurements were made using a Magnetic Property Measurement System (MPMS) by Quantum Design Inc. The MPMS is a magnetometer based on an extraction technique with superconducting coils. A SQUID (superconducting quantum interference device) is used to measure the induced current in the secondary coils. The MPMS allows a wide temperature range of 2K - 400K, and applied magnetic field capabilities of $\pm$5.0T. The measurements take place in vacuum, so samples must be dry. The MPMS allows for samples up to 9mm. In general though, samples are placed in a size 2 gel capsule.

Bulk magnetic measurements were used to study ensemble average properies of magnetotactic bacteria and iron loaded cells. This was used as a complement to single cell measurements techniques to check for consistency. It was also used as a first step as sort of a screening of samples before using other techniques.

Table 1.1 compares the the capabilities of the MPMS with other common bulk magnetometers. The vibrating sample magnetometer (VSM) works by measuring the induced voltage in pick up coils as the sample is vibrated sinusoidally inside a magnetic field. The alternating gradient magnetometer (AGM) is very similar, but uses an alternating magnetic field. The VSM and AGM have faster data acquisition times than the MPMS, but are less sensitive. However, MPMS can be combined with VSM to provide high sensitivity with fast data acquisition time [34].

Technique	Sensitivity	Measured Quantity	Pros	Cons
MPMS magnetic properties measurement system	$10^{11}\mu_B$ (10^{-8}emu)	M(H)	Large external field range Temperature range 1.9K - 400K	Slow data collection
VSM vibrating sample magnetometer	$10^{11}\mu_B$ (10^{-8}emu)	M(H)	Fast data collection	Sample position is unstable due to vibrations
AGM alternating gradient magnetometer	$10^{9}\mu_B$ (10^{-6}emu)	M(H)	Fast data collection	Limited mass capabiity

Table 1.1: Bulk Magnetometers

1.3.2 Electron microscopy for magnetic characterization

Electron microcopy can also be used for magnetic characterization. These techniques have very high spatial resolution and can be used to image within individual cells. Using different detectors in situ allows one to compare the magnetic images with traditional electron images of the same sample. However, the machines are expensive, difficult to use, and cannot cover a large spatial range in one experiment. Generally, these tools are ideal for looking at an individual cell, but not for looking at a large number of individual cells.

In addition, biological samples are a challeng to prepare for electron microscopy. The samples must survive ultra high vacuum conditions and must be treated to minimize charging and to enhance contrast. Larger cells must also be sectioned in order to see past the first few nanometers.

Electron holography

One of the most powerful techniques for measuring magnetism using electrons is electron holography. Electron holography is a derivative of transmission electron

microscopy (TEM) that is capable of measuring both the amplitude and phase of the transmitted electron wave [11]. An electron gun produces two beams of coherent electrons. One of these beams passes through the sample while the other (called the reference electron wave) does not. Past the sample plane, the two electron waves are recombined to form an intererence pattern, or hologram (Fig. 1.1).

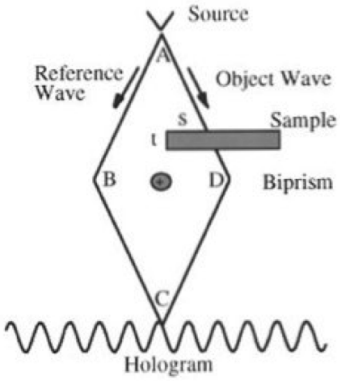

Figure 1.1: Schematic of electron holography [11]

The phase shift contains information about both the electric potential of the sample and its in-plane magnetization. The magnetic contribution can be isolated by various techniques. For example, one can invert the sample and acquire another hologam, or acquire two holograms at the same location with different microscope acceleration voltages.

Electron holography has be used to map out the strength and direction of local magnetization with 5-10nm resolution [32] [30]. An in situ magnetic field can be applied to study in-plane magnetic switching behavior. In combination with electron tomography, 3D reconstructions of the sample can be performed at the nanometer scale.

Sample preparation is one of the biggest challenges of using electron holography to study biological samples. Since electron holography is a transmission technique, samples must typically be <500nm thin. This allows single magnetotactic bacteria to be imaged [10], but not for whole mammalian cells which are roughly 10μm in size. In addition, the field of view is quite small, making it time consuming and difficult to image many cells at once.

Spin polarized SEM (SEMPA)

Spin-polarized scanning electron microscopy (SEMPA) is a form of SEM that uses a spin analyzer to detect electron spin polarization. When the electron beam of an SEM scans across a magnetic sample, the emitted secondary electrons are partially spin polarized. The direction and magnitude of this polarization is directly related to the magnitude and direction of the sample's surface magnetization [1]. SEMPA is capable of measuring topography and magnetization simultaneously and *completely separated*. However, this is a surface technique and can only probe the first 2-3nm of the sample.

Table 1.2 compares the capabilities of electron holography and SEMPA with some other common electron microscopy based magnetic characterization techniques.

1.3.3 X-ray techniques for magnetic characterization

X-rays can be used to measure magnetization because the absorption of synchrotron radiation is spin dependent above the K edge of $3d$ ferromagnets such as iron [40]. In the case of circularly polarized radiation, this is known as x-ray magnetic circular dichroism (XMCD). When circularly polarized photons hit a ferromagnetic surface, polarized photoelectrons are created in the unpolarized $1s$ state. Spin orbit coupling causes an energy splitting between $p_{1/2}$ and $p_{3/2}$ states, so the transition energy for these photoelectrons from s to p orbitals are spin dependent. Thus, the K-edge absorption coefficient contains a spin dependent term that is proportional to the difference in density between final photoelectron spin densities parallel and antiparallel to that of the ferromagnetic d electrons $\mu_c \propto \Delta\rho = \rho_{\uparrow\uparrow} - \rho_{\uparrow\downarrow}$.

In addition to measuring the K-edge absorption of $3d$ elements, one may also study the spin dependence of photoabsorption at the L-edge in $4d$ elements or M-edge in $5d$ elements. Because measurements are taken at these absorption edges, XMCD techniques allows for elemental contrast.

XMCD can also be combined with in-situ x-ray microscopy techniques for more

localized imaging with magnetic contrast. For instance, scanning transmission X-ray microscopy (STXM) with XMCD has been used to study the size dependence of magnetization reversal in Fe/Gd coated silica spheres ranging from 160nm - 800nm [3]. Photo-electron emission microscopy (PEEM) has been used to measure the XMCD spectra of single iron nanoparticles 6-25nm in size [36].

Table 1.3 compares these x-ray based techniques for magnetic characterization.

1.3.4 Magneto-optics

The magneto-optical effect describes the interaction of polarized light with a magnetic material, where time-reversal symmetry is broken. This time-reversal symmetry breaking causes orthogonally polarized light to propagate at different speeds. When light is transmitted throught the magneto-optical material, the result is a Faraday rotation of the plane of polarization. When light is reflected, it is called the mageto-optical Kerr effect (MOKE), or polar Kerr effect. Upon reflection, the polarization of the incident beam is rotated, and the angle between polarization axes of the incident and reflected beams is called the Kerr angle. The Kerr angle is proportional to the component of the sample's magnetic moment parallel to the incident light.

Magnetometers based on the magneto-optics have been used successfully for a variety of applications to measure nano-scale magnets. For instance, a MOKE magnetometer has been used to produce hysterisis loops of single 100-200nm magnetic nanowires [2]. Using an ultra-fast pulsed laser, time resolved measurements can be made to study magnetization dynamics on the femptosecond time scale [44].

In another variation known as the Sagnac effect, an interferometry technique is used to measure the Kerr or Faraday rotation. Using a "zero-area" closed loop and cryogenic temperatures, Sagnac interferometers have been shown to be highly sensitive magnetometers [45].

Table 1.3 compares magneto-optic techniques, along with X-ray techniques. It is important to note that magneto-optic magnetometers only measures the out-of-plane magnetic moment. For Kerr rotation measurements, the surface must be reflective,

and for Faraday rotation measurements, the sample must be sufficiently thin to allow light transmission.

1.3.5 Scanning SQUID magnetometry

Superconducting quantum interference devices, or SQUIDs, are sensitive magnetometers based on superconducting loops containing two Josephson junctions (Fig 1.2a). DC SQUIDs are based on the DC Josephson effect, which describes how screening currents form in the superconducting loop to cancel out external magnetic fields. When the current in either branch of the pickup loop exceeds the critical current I_C of the Josephson junction, a voltage appears across the junction. The critical current of the SQUID is a periodic function of the flux through the pickup loop, with periodicity exactly equal to the fundamental flux quantum, $\Phi_0 = h/e$. If we bias the SQUID above I_C, we can instead measure an oscillation in the voltage with the same periodicity.

The SQUIDs used in this work are designed specifically for scanning experiments and feature a gradiometric design with counterwound pickup loops (Fig 1.2b-d) [18]. One pickup loop is placed at the tip of a polished edge for scanning; the counterwound pickup loop is located far away from the tip to cancel out background magnetic flux. Superconduction shields placed aross the counterwound arms further screen background magnetic fields so that only flux passing through the pick-up loop is measured. Specific fabrication techniques and characterization are described in [23], and have been shown to have sensivity down to $100\mu_B/\sqrt{Hz}$.

While this technique has very high spin sensitivity, its spatial resolution is limited by the size of the pickup loops and the scan height. For experiments shown in this work, pickup loops are 3μm and typical scan heights are 2-5μm. In addition, because the flux image is a convolution of the magnetic flux with the pickup loop geometry, extraction of the magnetic field profile can be challenging.

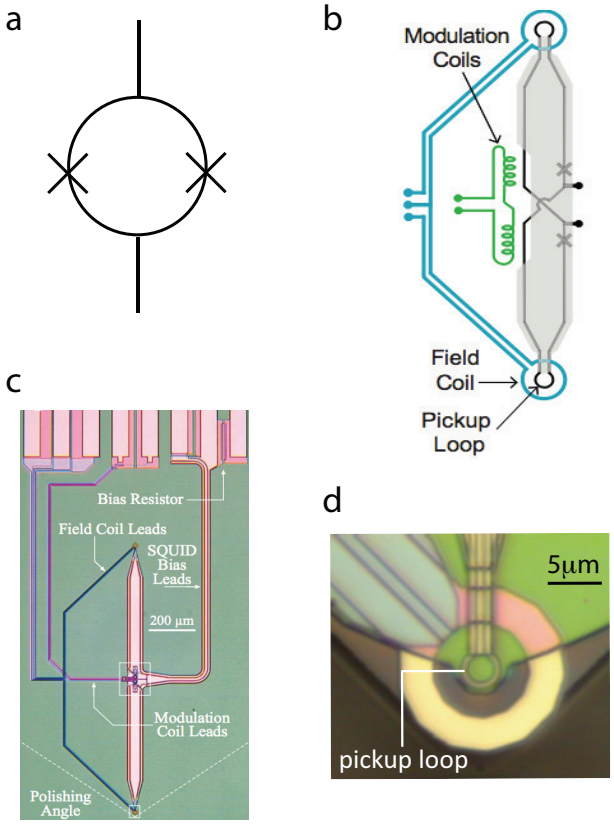

Figure 1.2: a) Schematic of a basic SQUID magnetometer. b) Modified SQUID for scanning used in the Moler group and in this thesis. c) Optical micrograph of scanning SQUID magnetometer/susceptometer [18]. d) Close up optical micrograph of pickup loop and field coil.

1.3.6 Magnetic force microscopy

Magnetic force microscopy (MFM) is a derivative of atomic force microscopy that uses a magnetic tip. Because magnetic forces are significantly longer range than atomic forces, if we scan a few tens of nanometers above a very smooth sample surface, we should theoretically be sensitive only to magnetic forces. This scan height, along with the tip radius, limits the spatial resolution of MFM. Reducing the scan height will increase spatial resolution, but the scan height must be much greater than the variations in sample height or else we will be measuring mostly topography.

For samples that are not perfectly smooth (but still reasonably flat), using two passes across each line can help isolate magnetic data from topography. In this technique, the first pass is performed in tapping mode where atomic forces dominate to obtain the topography of the line. Then we can lift a certain height z_0 called the *lift height*, and trace over the topography obtained from the first pass to measure the magnetic forces (Fig 1.3). Reducing lift height will provide higher spatial resolution and magnetic sensitivity, but will be more vulnerable to variations in sample height.

The spatial resolution and sensitivity of MFM is also limited by the size of the tip. Commercially available MFM tips have tip radii of roughly 60nm, and many research efforts have been aimed at reducing the tip radius [9] [24] [43] [46]. A smaller radius tip provides higher spatial resolution, but lower field sensitivity. Using commercially availble tips, MFM can achieve a spatial resolution of 50nm.

MFM is not ideal for imaging biological samples because the samples are not smooth. While there have been many advancements in imaging soft tissue with AFM, the results of using MFM to image magnetism in biological cells are not as promising as other techniques [33]. In addition, MFM is an invasive technique - if it is used to image "soft" magnetic samples with low coercivity, the magnetic probe tip can be strong enough to magnetize the sample.

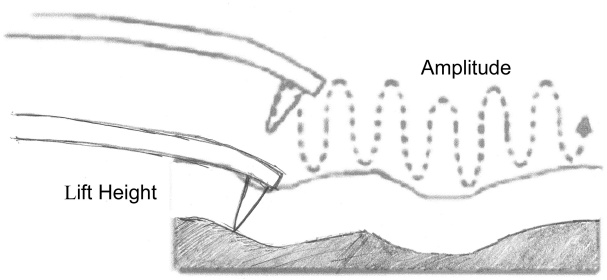

Figure 1.3: MFM operating in lift mode

Technique	Spatial resolution	Sensitivity	Sample Prep	Drawbacks	Advantages	What's measured
SEMPA	20nm	10^{-17}emu	Surface must be clean and conductive	1nm probing depth		Electron spin polarization
Electron holography	∼5nm	$0.003\Phi_0$	<500nm thick sections	Sample must be thin	Highest sensitivity and spatial resolution	Phase of transitted electrons
Lorentz microscopy	∼10nm		<500nm thick	Difficult to interpret quantitatively	Can measure large number of particles	TEM with magnetic contrast
SPLEEM	10nm		Clean, conductive surface	Surface study only	Good for thin films	Projection of magnetization vector onto electron polarization
SP-STM [41]	<1nm	$1\mu_B$	clean, conductive surface	Surface study only	Highest resolution	Local spin DOS

Table 1.2: EM techniques

Technique	Spatial resolution	Sensitivity	Sample Prep	Drawbacks	Advantages	What's measured
STXM + XMCD	25nm	few thousand atoms	Must by cryogenically preserved <100nm thin	Need x-ray source In situ sample preparation required	Elemental sensitivity Large external fields may be applied	Difference of x-ray absorption coefficients for right and left circularly polarized x-rays at absorption edge.
PEEM + XMCD	10-50nm	same	In situ cleaned so there is no oxide on surface	X-rays only penetrate 1nm into sample Quantitative interpretation difficult	Elemental sensitivity Time resolved	Photoelectron distribution emitted from surface, with magnetic contrast.
Sagnac Interferometer	30nm	$10^4\mu_B$	Surface must be reflective	Laser is usually narrow band	Can be used in scanning	Kerr rotation of reflected circularly polarized light
MOKE	1μm	6×10^{-12}emu $10^8\mu_B$	Surace must be reflective	Resolution limited by optical resolution	Can perform time resolved measurements using a pulsed laser	

Table 1.3: Xray and magneto-optical techniques

Chapter 2

Magnetotactic Bacteria

2.1 Introduction

Magnetotactic bacteria (MTB) were discovered in 1975 by Richard Blakemore. Blakemore observed microorganisms from marine marsh muds whose migration were directed by the earth's magnetic field [8]. These bacteria naturally grow have magnetosomes, magnetic mineral particles enclosed in membranes, and became known as magnetotactic bacteria. To date, all magnetotactic bacteria that have been discovered produce magnetic particles consisting of either magnetite (Fe_3O_4) or greigite (Fe_3S_4). Regardless of composition, the magnetosome particles are single domain and vary in size between 35nm - 120nm [5]. Each magneotactic bacterium represents a swimming permanent magnetic dipole, or biomagnetic compass.

MTB prefer anaerobic environements, and their ability to sense magnetic fields (called *magnetotaxis*) is believed to guide them to regions of optimal oxygen content. Magnetite-producing MTB are usually found in the transition zone between oxygen-rich and oxygen-poor water or sediment, where sharp chemical and/or oxygen gradients exist. Magnetotaxis is believed to allow the MTB to efficiently find an optimal position by simplifying a three-dimensional search to a one-dimensional problem [14].

Because of the bio-compatible membrane coating surrounding magnetosomes and the relatively narrow size distribution of magnetite particles, magnetotactic bacteria

have had some success in biotechnology applications [38]. In this chapter I will discuss the use of a particular strain of magnetotactic bacteria, AMB-1, for use as an MRI contrast agent. After an introduction of previous results using AMB-1, I will describe the work we did to measure the magnetic properties of individual bacteria. We studied two populations of AMB-1 that were supplemented with different iron sources, resulting in different average magnetic moments.

2.2 AMB-1 for enhancing MRI contrast

2.2.1 Previous work

Our involvement in characterizing individual magnetotactic bacteria began after a study by Benoit *et al* that showed the ability of *Magnetospirillum magneticum* AMB-1, a magnetite producing strain of magnetotactic bacteria, to provide positive magnetic resonance imaging contrast both *in vitro* and *in vivo* [6]. Because many bacteria are known to colonize the low-oxygen environment of tumors in mice following systemic delivery, the authors anticipated the ability of AMB-1 to provide simultaneous tumor targeting and magnetic resonance image contrast enhancement of the colonized tumors.

The authors in [6] grew all bacterial cultures from the same growth medium, but the iron was supplied either as ferric malate or iron chloride ($FeCl_3$). Alternating gradient magnetometry (AGM) measurements showed that cells supplemented with ferric malate were more magnetic than those supplemented with $FeCl_3$ by roughly a factor of three, and therefore had higher iron content per cell (Fig 2.1(a)). TEM images showed that these "high Fe" cells grown in ferric malate medium produced smaller magnetite particles than the "low Fe" cells grown in $FeCl_3$. However, although the mean particle diameters differed by a factor of two, both populations have wide distributions of particle sizes with a significant amount of overlap, as shown in Fig 2.1(b).

As described in Section 1.2.5, contrast agents work by locally altering the magnetic field in an MRI scan. They shorten the T1 (longitudinal) and/or T2 (transverse) time

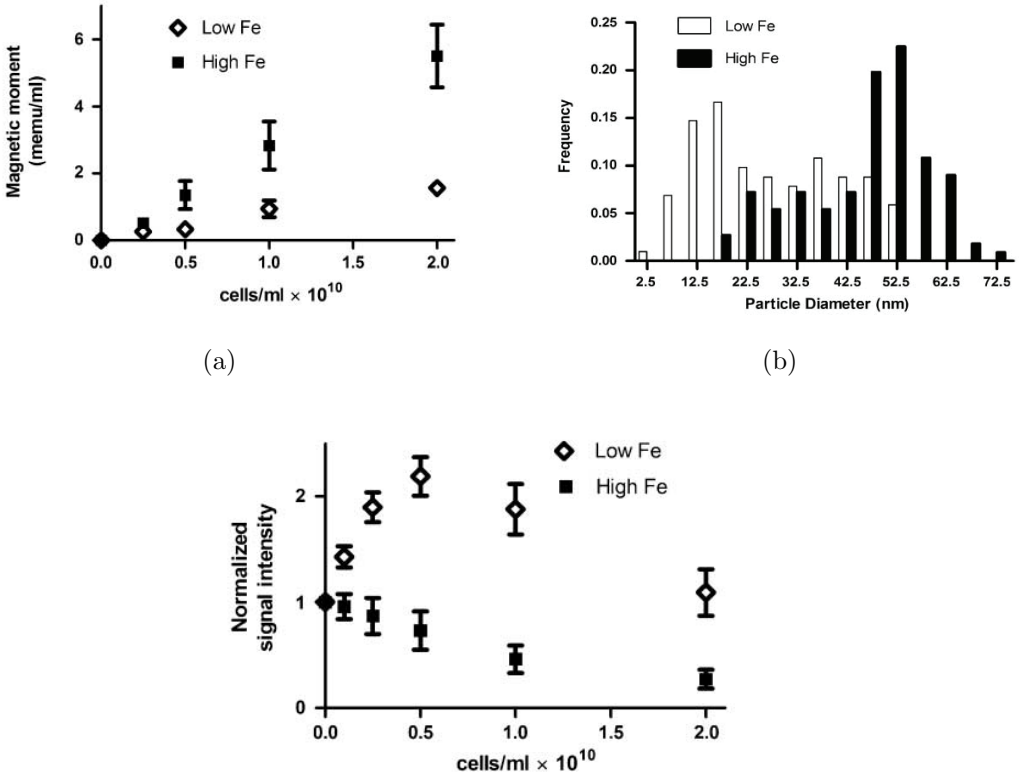

(a) (b)

(c)

Figure 2.1: **(a)**Magnetic moment of the two populations of AMB-1 as a function of cell concentration, measured by AGM. **(b)**Histogram showing the particle distribution for AMB-1 for both Low-Fe and High-Fe populations measured from TEM images of >100 particles per group. **(c)**Normalized in vitro MR signal intensities, showing how contrast enhancement of AMB-1 depends on Fe concentration. *Images taken from [6].*

of surrounding water protons, which results in brighter signals (positive contrast) or darker signals (negative contrast), respectively. Magnetic resonance measurements were made at 3T both *in vitro* (on phantoms) and *in vivo* (on mice tumors). The authors found that all magnetite carrying AMB-1 provided negative image contrast in T2-weighted images, with signal intensity decreasingly linearly with cell concentration. This is typical of superparamagnetic contrast agents. However, the authors also discovered that "Low-Fe" AMB-1 supplemented with $FeCl_3$ produced positive contrast in T1-weighted images. As show in Fig 2.1(c), the positive contrast begins at a cell concentration of 0.25×10^{10}/mL, becomes more intense at 0.5×10^{10}/mL, with the AMB-1 loaded tumor generating nearly twice as signal as the control sample. The positive contrast decreases with further increase in concentration as the T2 effect begins to dominate. No positive contrast was observed for "High-Fe" AMB-1 grown in iron malate. This result indicates that the ratio of the transverse to logitudinal relaxivities, r_2/r_1, is higher for the "Low-Fe" AMB-1 that have smaller magnetite particles and lower magnetization than for the "High-Fe" AMB-1.

2.2.2 Need for single cell magnetic characterization

Our goal is to further investigate how the differences in magnetic properties between these two AMB-1 populations lead to such differing MR signals. Is this difference in signal due to a small fraction of bacteria with unique magnetic properties within the large number that are used to obtain each image? Although the AGM measurements in [6] show a clear difference in average magnetization between AMB-1 grown with iron malate versus $FeCl_3$, we are interested in the distribution of magnetizations of single cells within each population and how they compare to distributions of magnetite particle size observed in Figure 2.1(b). Such information will provide insight into how to optimize contrast agent properties and pulse sequences for optimal MR signal contrast.

In the next chapter, I will discuss how genetically encoding cancer cells with the iron uptaking capabilities of magnetotactic bacteria has potential to improve diagnostic abilities and provide single cell MRI tracking. If we wish to study the

MR signal coming from individual magnetite carrying cells, it is essential to study the magnetic properties of individual cells. We wish to measure the distribution of magnetic properties among a population of cells with the same growth conditions, and study how magnetic properties of single cells affects their resulting MR signal.

We will perform this study using scanning SQUID magnetometry and susceptometry, using SEM and bulk magnetometry to check for consistency. In the remainder of this chapter, I will cover methods and results. In Chapter 4, I will describe how we calculated dipole moments from scanning SQUID magnetometry images.

2.3 Materials and Methods

In this section I will cover how our bacterial samples were grown and prepared for various magnetic characterization techniques.

2.3.1 Bacterial growth and preparation

The AMB-1 bacteria we studied were grown according to [6]. AMB-1 are grown from a glycerol stock. To initiate culturing a 15mL starter culture is made and grown without iron supplementation for six days, at 30°C with modified *Magnetospirillum* growth medium (MSGM) supplemented with 150μg of Vitamin solution. Cultures were grown in sealed tubes with 7% headspace of air.

After six days, iron-free or iron-supplemented cultures were set up. Iron-poor supplementation consisted of 40μmol/L of precipitated $FeCl_3$. Iron-rich supplementation consisted of 40μmol/L of ferric malate. Iron-free cultures for use as control samples were resuspended in MSGM without iron supplementation. All samples were sealed in tubes with 7% air space and left for six days without shaking at 30°C.

After the final six days of culture, the contents of each tube were spun down in a centrifuge at 8000g for 15 minutes. Each pellet was washed twice in high grade water and then resuspended. Cell density was determined by optical density measurements (using a Shimadzu BioSpec-1601 spectrophotometer) correlated to a standard curve.

A portion of each bacterial sample were fixed using 2.5% glutaraldehyde in 0.1M

cacodylate buffer. Bulk magnetometry measurements made with MPMS did not show any difference in net magnetization between fixed and not fixed cells, although the coercivity at 4K is slightly larger for fixed cells (see Section 2.4.1). SEM images of several bacteria from each population showed no visible differences in magnetite particle size or chain behavior between fixed and not fixed cells. In scanning SQUID experiments, we found that the fixative generated large susceptibility signals that were hard to differentiate from those from the magnetite particles. In addition, the MRI contrast observed in [6] were made using live AMB-1 cells that have not been fixed. Due to these reasons, we ultimately chose to perform our experiments using bacterial cells that have not been fixed.

Cells from each iron supplement condition (High Fe, Low Fe, No Fe) were suspended in high grade water at a density of 2×10^9 cells/mL and stored in Eppendorf tubes at 4°C for up to one month. The sample preparation for each of the characterization techniques we used are described below.

2.3.2 Bulk magnetometry

For bulk magnetometry measurements using MPMS, bacterial cells were first transferred to ethanol and then spun down into pellets at the bottom of a gel capsule. The procedures are as follows:

1. Vortex solution and transfer desired volume of cells into Eppendorf tube.
2. Spin for 5 minutes at 4000rpm to form pellet
3. Remove solvent taking care to not remove any cells, and suspend in 50% Ethanol for 10 minutes
4. Spin for 5 minutes at 4000rpm to form a good sized pellet
5. Repeat steps 3 and 4 with 70%, 95%, and 100% (2x) ethanol.
6. Add about 5μL EtOH to resulting pellet, mix by repeatedly pipetting the solution, then transfer to gel capsule.

7. Place capsule into dry Eppndorf tube and centrifuge until there is a pellet at bottom of capsule. Pipette out remaining solvent, and allow any remaining solvent to dry in fume hood.

Once samples are prepared, a pinhole was punched at the top of the gel capsule to allow air to escape. The gel capsule is then placed inside a straw, which is a standard way of mounting samples to the MPMS insert.

DC hysterisis curves were taken at 5K, which is the temperature at which the scanning SQUID measurements are taken at.

2.3.3 Scanning SQUID

For navigation purposes, bacteria are dispersed onto a silicon substrate with a gold meander pattern.

Cells are diluted to roughly a concentration of 10^5 cells/mL in ethanol, and dispersed drop by drop onto the chip until a desired concentration was achieved. Ideally, the bacteria would be spread out evenly across the surface, 5-10μm apart from each other so that they could be imaged individually. Of course this is not possible to achieve. We observed that the cells often dried near the corners of the meander grids and sometimes formed clumps.

After the substrate is dried, it is glued onto a copper sample mount using GE varnish, and electrical connections are made to the meander using aluminum wire bonds. A superconducting sample is usually mounted on the sample mount next to sample, with care taken to have the surface plans be parallel and at the same height. The samples are mounted onto the microscope scanner, which is then placed under vacuum and cooled down in a liquid helium cryostat.

2.3.4 Electron microscopy

Whole bacterial cells were studied using SEM. Using a back scatter detector (on FEI Magellan) at 5keV accelerating voltage and 10nA gun current, the magnetosomes were clearly visible. Using the CBS (backscattered electron) detector, we can achieve

a penetration depth of up to 1μm, so the entire depth of each bacterium can be probed.

Samples were not plasma cleaned, as this resulted in cell damage.

2.4 Results

2.4.1 Bulk magnetometry

DC hysterisis curves were obtained at 5K, after bacterial pellets were prepared according to Section 2.3.2. Iron rich and iron poor bacteria were grown according to protocol from [6], and we used the MPMS to perform initial characterization. Due to issues with bacteria growth, the first several cultures did not show any difference in magnetization between iron rich and iron poor growth conditions. Fig. 2.2 shows the first growth with a clear difference in magnetic signal between the two types of iron supplementations.

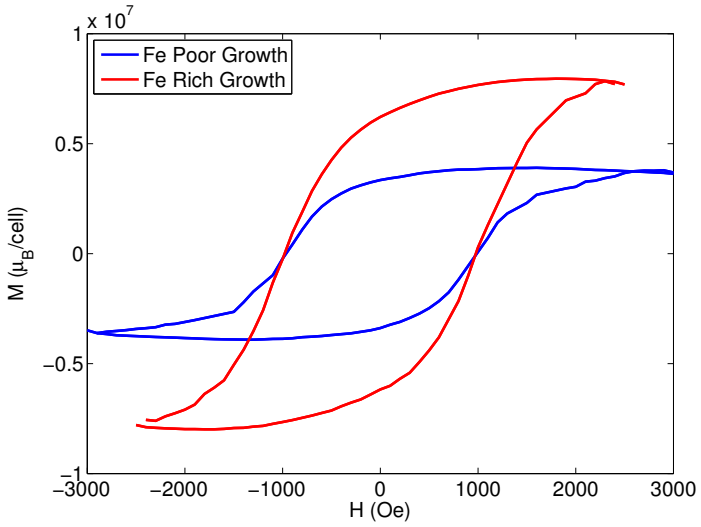

Figure 2.2: MPMS measurements of AMB-1 bacteria grown with either high iron (ferric malate) or low iron (iron chloride) supplementation, taken at 5K. Roughly 5×10^8 cells were used for each pellet.

We used roughly 5×10^8 cells for each measurement. The results show that

the saturation magnetizations for iron rich and iron poor bacteria populations are $7.5 \times 10^6 \mu_B$ per cell and $3.8 \times 10^6 \mu_B$ per cell, respectively. In comparison, bulk magnetometry on similarly grown bacteria studied in [6] are roughly $2.5 \times 10^7 \mu_B$ per cell and $1.0 \times 10^7 \mu_B$ per cell. We note that for our samples, although the iron rich bacteria are roughly twice as magnetic as the iron poor bacteria, the magnitude of the saturation magnetization for either population are more than three times less than those studied in [6] (Fig. 2.1(a)). This indicates that the iron uptake of the bacteria we studied are very different from the ones studied in [6].

We also note that the widths of the two curves in Figure 2.2 are the same, indicating that the coercivities of the two bacterial populations are the same and that the form of iron is likely to be the same. The shape of the curves - in particular, the the shallow slope of the curves before hitting saturation – indicate that the magnetization vector is not switching uniformly throughout each population.

2.4.2 Electron Microscopy

SEM and TEM was used to image numerous bacteria from both Fe poor and Fe rich populations. Some typical images are shown in Fig 2.3(a)- 2.3(c).

From our limited data set (we studied ~ 200 bacteria from each population with SEM and ~ 10 bacteria from each population with TEM), we estimated that roughly 60-70% of bacteria in both populations have empty magnetosomes, meaning they did not uptake iron and form magnetite particles. This could explain the discrepancy in the average moment per cell between the bacteria studied in [6] and the ones we measured in 2.2.

In addition, we observed that most of the magnetosome-containing bacteria contained disjoined chains. Instead of a single chain of coupled magnetite particles, the bacteria contained several short, broken chains of magnetosomes and often single particles not a part of a chain. This could be an indication of incomplete incubation or incomplete iron uptake [13].

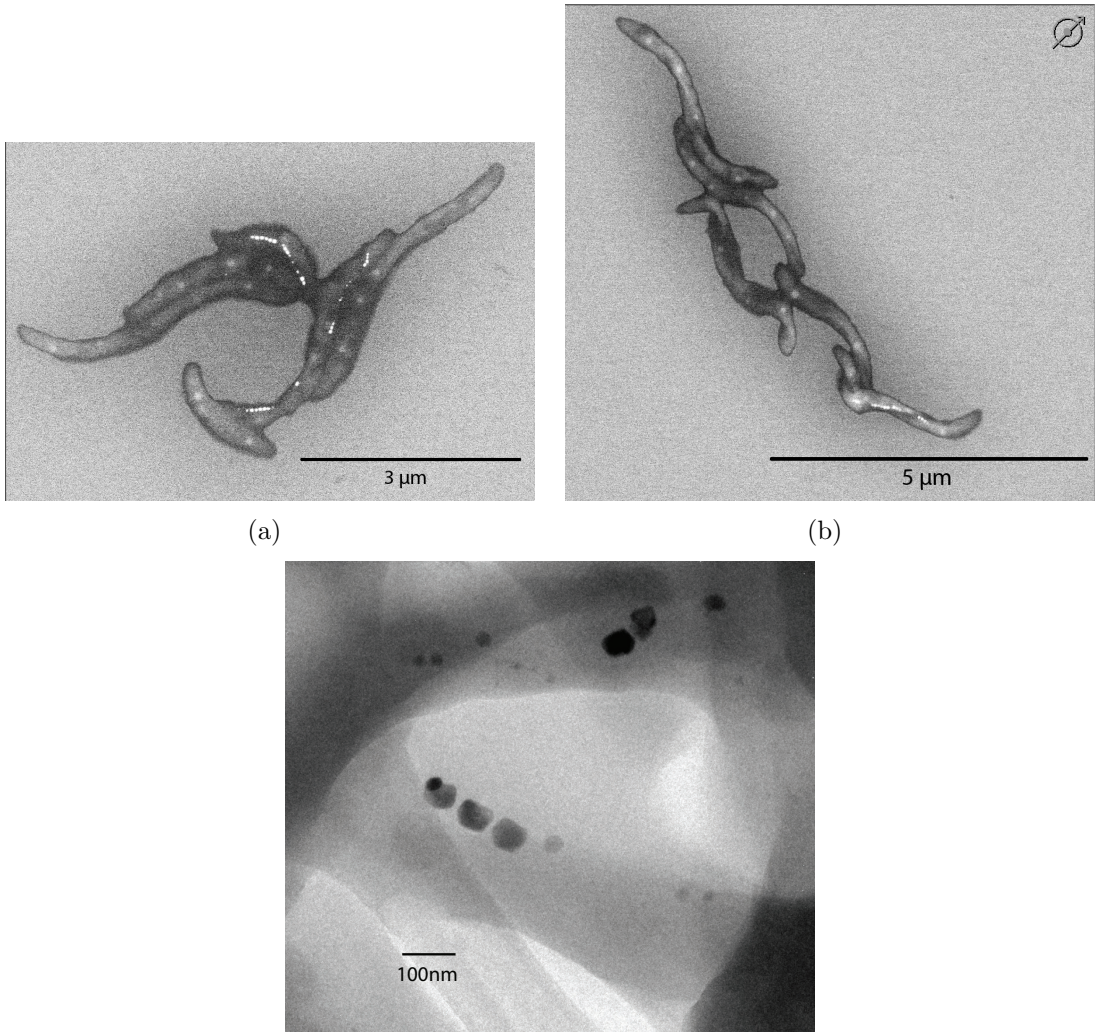

(a) (b)

(c)

Figure 2.3: **(a)**SEM of a random selection of bacteria from the Fe rich population. Magnetosomes are visible as bright spots. **(b)**SEM of a random selection of Fe poor bacteria. **(c)**TEM image of a random Fe Rich bacteria showing close up of magnetosomes.

2.4.3 Scanning SQUID

After the samples are prepared according to 2.3.3, scanning SQUID magnetometry measurements were performed over as much of the sample as possible. The scan range for each image is roughly 100μm$\times100\mu$m, and the Attocube positioners allow for up to 5mm$\times$5mm of total range. Locking into an AC current applied to the meander allows us to accurate determine the location and match up magnetic signals with magnetotactic bacteria that produced them.

FIgure 2.4.3 shows corresponding susceptometry data of a grid, DC magnetometry data of the bacteria containing sample, and SEM images of the substrate. Select SEM images of magnetotactic bacteria are shown, matched with their magnetometry signals. This technique can also be used to identify empty bacteria, or bacteria not containing any magnetosomes, by locating bacteria that do not have measurable magnetometry signals. This can be further confirmed by using SEM to image within the cell.

From these magnetometry images, we crop out individual dipoles and calculate their dipole moments using a superconducting vortex image obtained from the same cooldown using the same SQUID and the fitting technique described in Chapter 4. We count empty bacteria, but do not include bacteria whose dipoles are spaced too closely together to be individually resolved and analyzed.

Figure 2.5(a)shows a histogram of the moments of 151 iron rich bacteria and 137 iron poor bacteria. We see that 60-70% of each population are empty or otherwise have no matching magnetometry features corresponding to bacteria on the sample. Figure 2.5(b)shows the same plot with zeros removed and moments binned on a logarithmic axis. From the histograms we see that the range of moments for both populations span two orders of magnitude and have considerable overlap. However, averaging together the moments for the measured bacteria, we obtain a mean of $2.13\times10^6\mu_B$/cell for the iron rich bacteria and $1.01\times10^6\mu_B$/cell for iron poor bacteria. So although there is a factor of two difference in the average moment/cell between the two population, there is so much spread that just from looking at the magnetization of a single bacterium, there is no way of telling which population it belongs to.

We note that the mean moments/cell we obtained from measuring individual

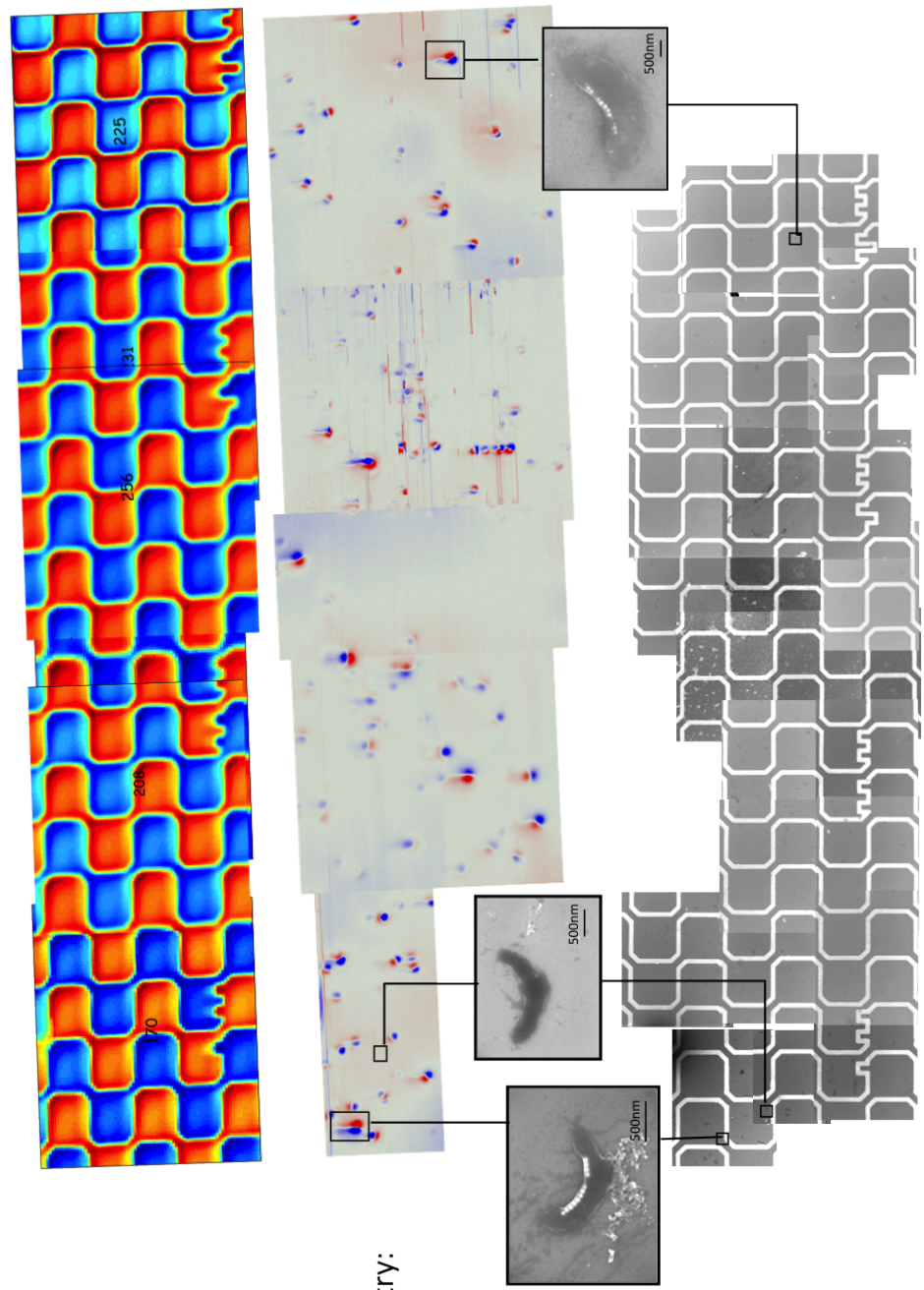

Figure 2.4: Corresponding scanning SQUID susceptometry (top panel), magnetometry (middle panel) and SEM (bottom panel) of substrate containing magnetotactic bacteria and gold meander grid for navigation.

bacteria are significantly lower from the estimate of the saturation magnetization/cell of the same bacterial populations obtained from MPMS ($7.5 \times 10^6 \mu_B$/cell and $3.8 \times 10^6 \mu_B$/cell). This is most likely due to the fact that the magnetosomes did not form a neatly coupled chain in the bacteria, but instead were broken up. For scanning SQUID measurements, we cannot apply a large external field and did not cool down in field. Therefore most likely the magnetosomes in each bacterium are not magnetically coupled to each other and therefore are not at their full magnetization at zero field. If we were able to apply a large field, or if the chains were better formed, the measured moment per cell would be larger and closer to the values obtained through MPMS measurements. Nevertheless, our results show that scanning SQUID is a powerful, non-invasive tool that can be effectively used to characterize the magnetic properties of individual magnetotactic bacteria.

2.5 Conclusions

From these results, we can conclude that:

1. Scanning SQUID can be used to quantitative measure the magnetic moment of individual magnetite carrying bacteria.

2. The magnetic properties of individual bacteria differ significantly amongst a population, and this distribution is not directly apparent in bulk measurements.

3. While the two different populations of bacteria studied here have different average magnetic moment, individual moments overlap to a great degree. From looking at a single bacterium, there is no way of telling which population it is from.

4. Because of the large number of empty magnetosomes (bacteria that did not form magnetite) in both populations and the difference in chain morphology from magnetotactic bacteria cited in literature, the bacteria used in this study most likely suffered from incomplete growth and is not directly comparable to the ones used for enhancing MRI contrast in [6].

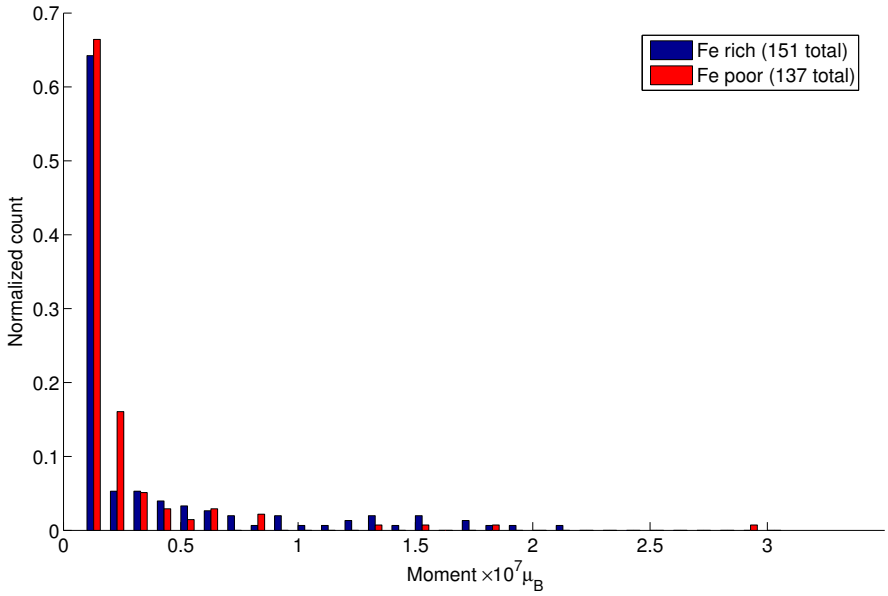

(a)

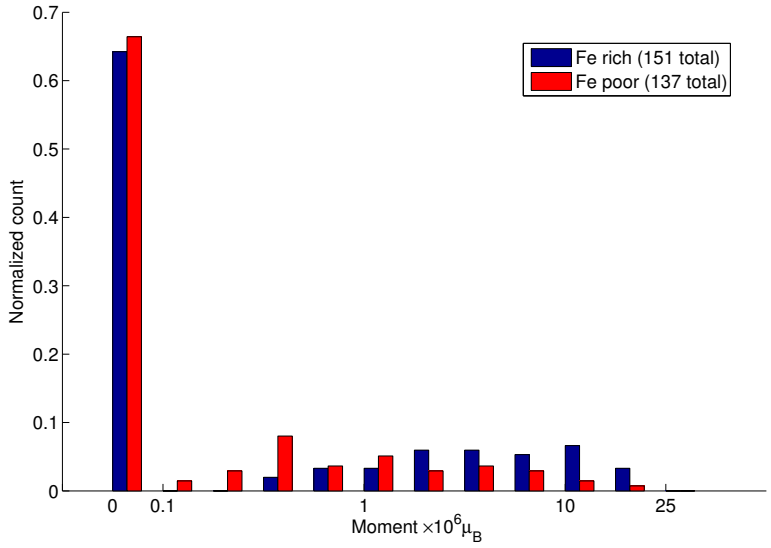

(b)

Figure 2.5: **(a)**Histogram of all bacteria with matching bodies. **(b)**Histogram of same bacteria, plotted on log axis. Mean values are $2.13 \times 10^6 \mu_B$/cell for the iron rich bacteria and $1.01 \times 10^6 \mu_B$/cell for iron poor bacteria.

5. While we cannot conclude anything about how the magnetic properties of individual bacteria influenced the MRI contrast in [6], we have identified single cell magnetic imaging as an important component of characterization for single cell biomedical applications.

Chapter 3

Mammalian Cells

Using magnetotactic bacteria as a naturally tumor targeting contrast agent is interesting but unlikely to become clinically approved. In this chapter I will describe an ongoing effort to develop single cell MRI technology using genetically encoded iron based reporters by expressing bacterial genes in mammalian cells.

3.1 Introduction

Having a genetically encoded contrast agent in cancer or stem cells could improve the usefulness of MRI in cancer diagnosis or stem cell transplantation. Stem cell transplantation, similar to gene therapy, involves the infusion of healthy stem cells to replace damaged or diseased stem cells. In order for this to become a clinically approved therapy, methods to non-invasively monitor stem cells in patients must be developed.

Several studies have shown the ability for MRI to track cells preloaded with SPIO contrast agents. But this sort of labeling can result in several drawbacks. For instance, cell division can lead to dilution of SPIO particles and thus loss of signal. In addition, false signals can be detected from dying or dead cells. A genetic labeling approach has the potential to overcome these obstacles. This would result in an endogenous and persistent generation of cell contrast, and would be valuable to stem cell therapy or detecting cancer cells. In addition, recent advances in MRI technology has allowed

single cell detection and tracking [16] [17]. If the cells could uptake enough iron, these MRI technologies could be used to track the viability and function of very small numbers of cells.

A recent study has shown that magA, a gene in magnetotactic bacteria known to be involved with iron transport, can be expressed in a human cell line [47]. This resulted in the human cells producing iron-oxide nanoparticles similar to the magnetosomes produced by bacteria. These endogenously generated iron oxide particles were successful in providing image contrast in T2-weighted MR images.

The goal of this project is to similarly express bacterial genes responsible for iron transport in mammalian cells to create a genetically encoded MRI reporter, with the eventual goal of single cell tracking and detection via MRI.

Our role in this project is to use our experties in magnetic characterization study the magnetic properties of these cells individually to help in optimizing iron uptake.

3.1.1 Progress

So far, the main road block of the project has been to successfully express the bacterial genes into a mammalian cell line. The two genes that have been the focus of the work so far are magA and mms6, although many other bacterial genes are involved in iron uptake and magnetosome formation. The mammalian cell line we have been working with is MDA-MB-231BR, a breast cancer cell line that metastasizes in the brain. While there has been some evidence of increased iron accumulation in vitro with these two genes, the results have not been reproduceable and no success has been reported in vivo. Furthermore, it is unclear whether this is because the gene is not actually being expressed or if the gene is not sufficient for iron uptake.

Due to these struggles, we have not been able to characterize any genetically expressed cells. However we have worked to develop protocols for magnetic characterization by using SPIO labeled mammalian cells. These are 231BR cells that have been labeled with either Molday or Bangs Beads. These are two types of commercially available, fluorescently labeled, SPIO particles that are functionalized to be easily absorbed by cells. In the next section I will describe how we prepare these cells

for characterization.

3.2 Sample preparation for magnetic characterization

The main difficulty in preparing mammalian cells for our characterization techniques is in the size of the mammalian cells. They are not uniform in size and vary between 5μm to 30μm, compared to magnetotactic bacteria which were generally 1-3μm long and a few hundred nanometers in width. Their large size and nonuniformity means that we cannot simply disperse the cells on a substrate and perform scanning experiments at or near contact. It also means that we cannot use electron microscopy (SEM/TEM) to image within an entire cell and locate magnetic nanoparticles.

3.2.1 Samples

The mammalian cells we studied were MDA-MB-231BR, a line of brain-metastasizing breast cancer cells. To develop protocols to study these mammalian cells, we studied an array of nanoparticle labeled cells of different label types and concentrations. 231BR cells were labeled in vitro with 6, 12, or 24 μg Fe/mL of either Bangs-Flash Red or Molday ION nanoparticles.

6×10^6 cells of each type were labeled, thoroughly washed and then fixed with 2.5% glutaraldehyde and 1% osmium tetroxide. In addition, we were also provided with control 231BR parent cells, control magA-labeled 231BR cells, and 1.5mM FN supplemented magA-231BR cells.

3.2.2 Bulk Magnetometry

For bulk measurements using MPMS, samples were dehydrated, transferred to ethanol and spun down in gel capsules as described in Section 2.3.2. Because cell loss is inevitable during the dehydration and transfer process, we made two pellets for each sample that nominally contain the same number of cells (1.2×10^6 cells per pellet).

By making measurements on both pellets, we can get an idea of the errors associated with inaccurate cell count when using MPMS to calculate the average dipole moment per cell.

Figure 3.1 shows what a pellet looks like at the bottom of the gel capsule after the remaining solvent has been evaporated. The pellet is black in color due to the osmium fixative.

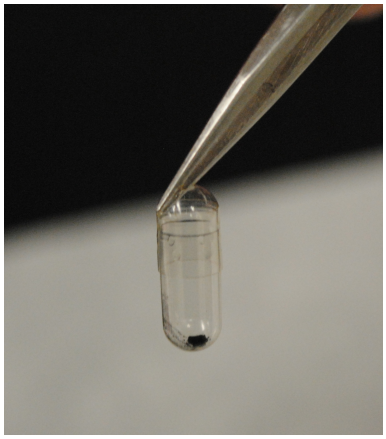

Figure 3.1: Photograph of pellet of 231BR cells for use in MPMS measurements. This pellet contains roughly 1.2×10^6 cells and is black due to osmium fixative.

3.2.3 Electron microscopy

In order to perform SEM/TEM, cells must be Epon infiltrated and embedded, then sectioned using an ultramicrotome. To aid in image contrast, we stained the cells with 1% Uranyl acetate, a negative stain. We followed the standard Epon infiltration process provided by the Cell Sciences Imaging Facility (CSIF) at Stanford. The infiltrated cells were then placed in molds, labeled, and filled with 100% Epon, and finally polymerized for 24 hours at 65°C.

The polymerized cells can be stored at room temperature for many months. They can be sectioned using an ultramicrotome and placed onto TEM grids (for TEM) or silicon substrates for SEM. Sections should be no more than 80nm thick for TEM, but can be thicker for SEM.

3.2.4 Scanning SQUID

Because the mammalian cells are 5-30μm in diameter and non-uniform in size, they cannot be deposited onto a silicon substrate containing a gold meander for scanning SQUID magnetometry. As a first step, we took 400nm thick sections of Epon embedded cells and placed them on the same substrates that we used for measuring magnetotactic bacteria (Fig. 3.7). However, since the SPIO particles are not evenly distributed within each cell, measuring a 400nm thick section does not allow us to extract the total magnetic moment of a cell.

In order to use scanning SQUID to image whole cells, we must overcome the topography issues that the large and non-uniformly sized mammalian cells present. To do this, we deposited cells onto a silicon nitride membrane window and then performed scanning measurements on the reverse side of the window. SiN membrane windows are commonly used for electron microscopy applications and can be purchased commercially from companies such as Ted Pella (Fig. 3.2(a)). We used a 1mm$\times$1mm window, which is the largest area window supplied by Ted Pella, with a 200nm thick membrane, which was emperically determined to be the thinnest possible membrane that is able to withstand our techniques.

To aid in navigation, we also patterned a gold meander onto the backside of the SiN membrane using standard photolithography techniques slightly modified to accomodate the mechanical flexibility of the membrane. The SPIO labeled 231BR cells were then diluted in ethanol and pipetted into the well one drop at a time until the desired concentration was achieved. Because the membrane is transparent to visible light and both Molday ION and Bangs Beads particles are fluorescently labeled, corresponding fluorescence and optical images can be taken to determine precisely which cells contain SPIO particles (Fig. 3.2(b)).

3.3 Results for SPIO loaded cells

In this section, I will discuss the results of our measurements on SPIO loaded cells and address a few problems we are facing.

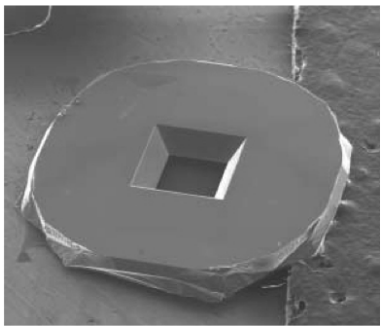

(a)

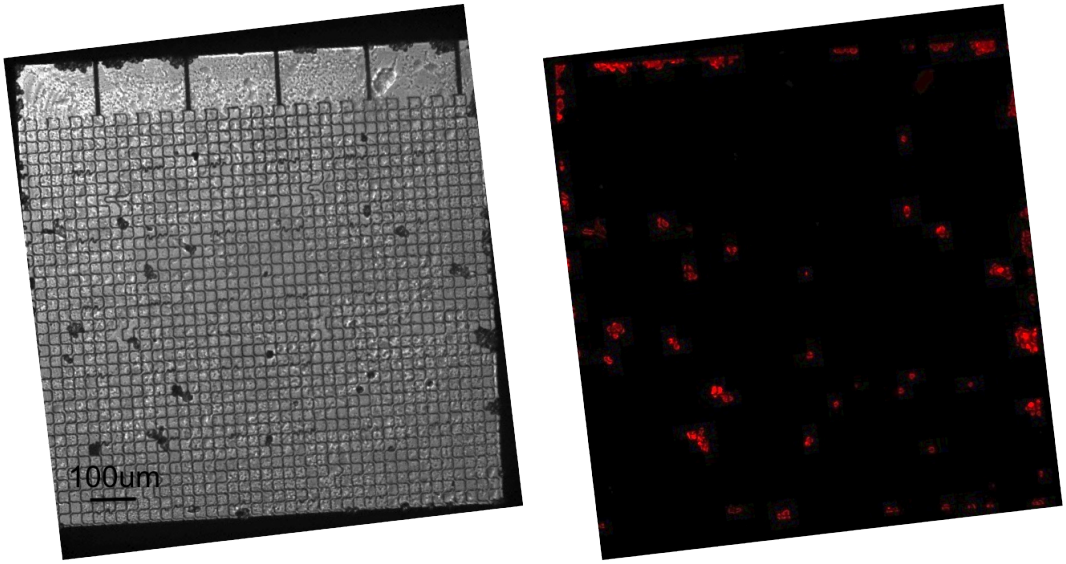

(b)

Figure 3.2: **(a)**Silicon nitride membrane window. Image from www.2spi.com/catalog/grids/silicon-nitride.php. **(b)**Optical micrographs (left) and corresponding fluorescence images (right) of Molday ION labeled 231BR cells deposited onto membrane with gold meander pattern for navigation.

3.3.1 Bulk magnetometry

We used a Quantum Design MPMS to measure hysterisis curves of each cell sample in bulk at 10K, which is roughly the temperature the scanning SQUID measurements will be taken at. Fig. 3.3 shows the results of these measurements. As described in Section 3.2.2, we made two pellets of each sample, each containing nominally 1.2×10^6 cells, to account for some of the uncertainty in cell count. Each curve in Fig. 3.3 is the average of measurements taken on both pellets corresponding to that sample. We found that the saturation magnetization between each pair of pellets varied up to 20%, a difference that is due to sample preparation.

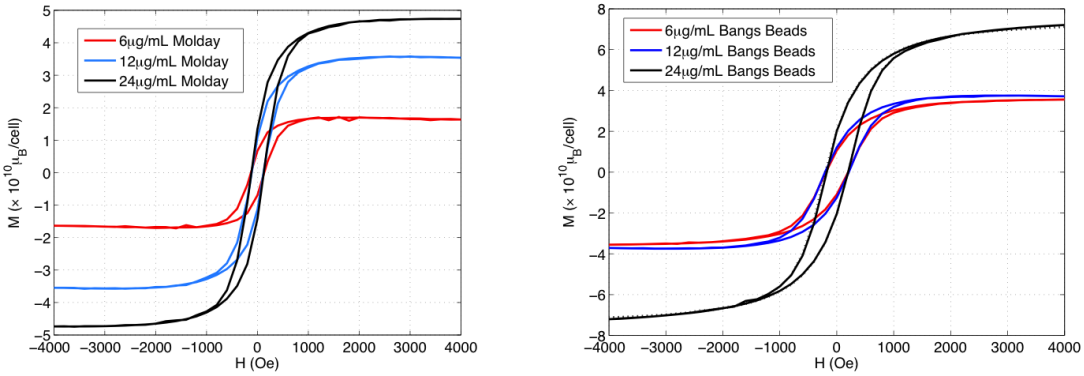

Figure 3.3: Hysterisis curves of SPIO loaded 231BR cells taken at 10K. Molday ION loaded cells of various loading concentrations are on the left; Bangs Beads loaded cells are on the right. Each curve represent the average of measurements taken on two pellets that nominally contain the same number of cells. All pellets nominally contain 1.2×10^6 cells.

Fig. 3.3 shows that Bangs Beads loaded cells have a higher saturation magnetization than Molday cells by roughly a factor of two. For both types of SPIO, a higher loading concentraion results in higher saturation magnetization. However, the relationship is not linear. We also note that the magnetic coercivity is consistent across loading concentrations and that at 10K, cells loaded with Bangs Beads have a larger coercive field than cells loaded with Molday. Fig. 3.4 shows that both types of cells are paramagnetic at room temperature.

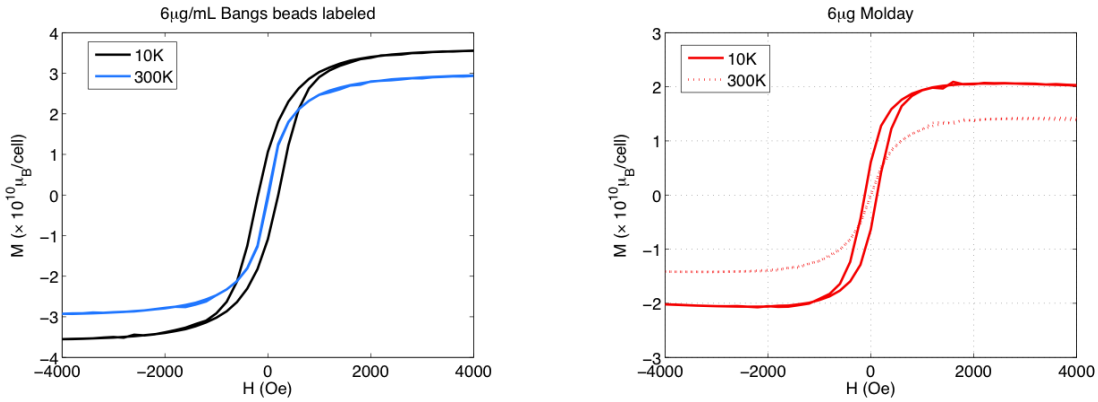

Figure 3.4: Comparisons of hysterisis curves of SPIO loaded 231BR cells taken at 10K and at 300K.

To determine blocking temperature T_C, below which hysterisis sets in for the superparamagnetic particles, we performed zero field cooled (ZFC) temperature sweeps. These measurements are done by first warming the sample up to 300K in zero field, where the cells are now completely unmagnetized. Next, a small field (10 Gauss) is applied and the sample is cooled down to 10K where the cells are ferromagnetic. Then in this small field, we slowly increase in the temperature back up to 300K and measure the magnetization along the way. Fig. 3.5 shows that Bangs Bead labeled cells have a much higher blocking temperature than Molday labeled cells.

3.3.2 Electron Microscopy

We performed SEM on sections of cells prepared using techniques outlined in the previous section. The best images were taken using a back scatter electron detector. Because the cells have been stained, we used the built-in EDS detector to perform energy-dispersive x-ray spectroscopy (EDS) and ascertain where the iron containing SPIO particles are located within each cell section.

As Fig. 3.6(a) shows, the SPIO particles are not spread uniformly throughout the cell but instead contained in organelles a few microns in size. Although the image in Fig. 3.6(a) only shows one of these islands, we often see sections that contain multiple clusters of particles. This implies that each cell can contain multiple islands

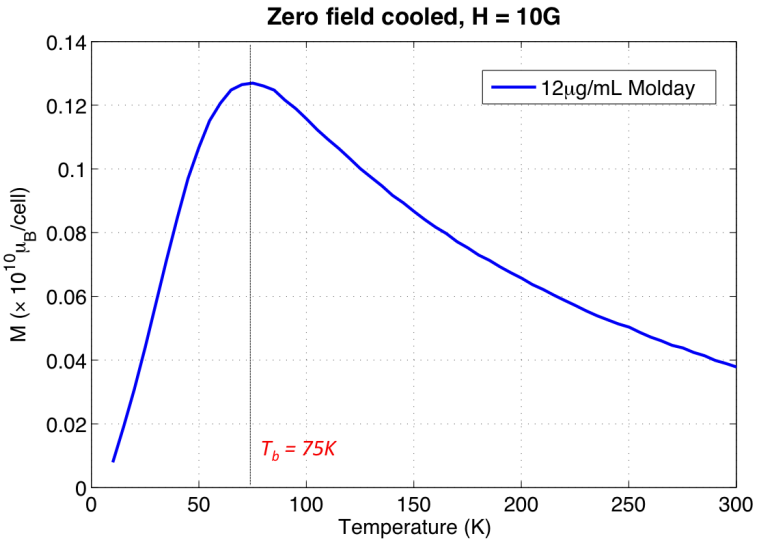

(a)

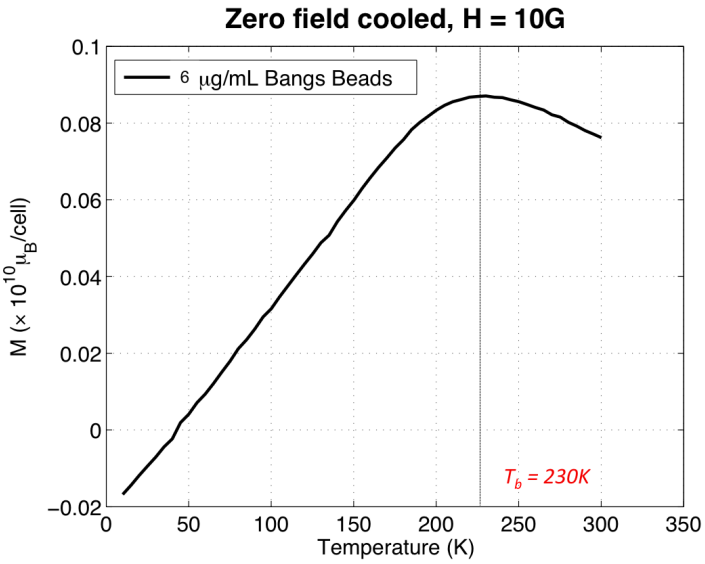

(b)

Figure 3.5: Zero field cooled temperature sweeps to measure blocking temperature of cells containing superparamagnetic particles. **(a)**ZFC measurements of Molday labeled cells show a blocking temperature of 70K. **(b)**Bangs Bead labeled cells have a much higher blocking temperature of 230K.

of SPIO particles spaced several microns apart. This observation is consistent across cells loaded with both Molday and Bangs Beads particles, and across all the loading concentrations that we studied.

3.3.3 Scanning SQUID magnetometry

As an initial step, we performed scanning SQUID measurements on thin sections of cells that have been infiltrated with and embedded in Epon epoxy. After embedding and sectioning according to Section 3.2.3, the 200nm - 400nm thick sections were transferred onto a silicon substrate containing a gold meander. After scanning SQUID magnetometry measurements were taken, the cell section containing chip was treated with toluidine blue stain so that the cells become easily visible. An optical image of the post-processed sample and its corresponding scanning SQUID magnetometry image are shown in Fig. 3.7. The area of sample covered by scanning SQUID measurements is outlined on the optical image. On the right, the grid susceptometry image is overlaid on the magnetometry image to allow for locating features. Corresponding dipole signals on the magnetometry image that can matched to the physical locations of cells are circled.

Fig. 3.7 shows that nearly all of the cell sections can be matched to a magnetic signal in the SQUID magnetometry image. However, we are interested in obtaining the magnetic dipole moment of a single cell. Since the sections represent only a 400nm slice through a 5-25μm cell and the magnetic SPIO particles are not predictably distributed throughout the cell, there is no way of determining the magnetic moment of the entire cell from these measurements. Moreover, we notice that the magnetic signals that we measure from these cell sections are not point dipole-like, but have strong quadrupole moments. This is most likely because the SPIO particles are clustered together in clumps a few microns in size (Fig. 3.6(a)), which is about the same size as the SQUID pick-up loop. Therefore these clumps cannot be approximated as point dipoles. Moreover, there can be several of these clusters within a cell, meaning they are not magnetically coupled but are still too close to be resolved by tbe pick-up loop.

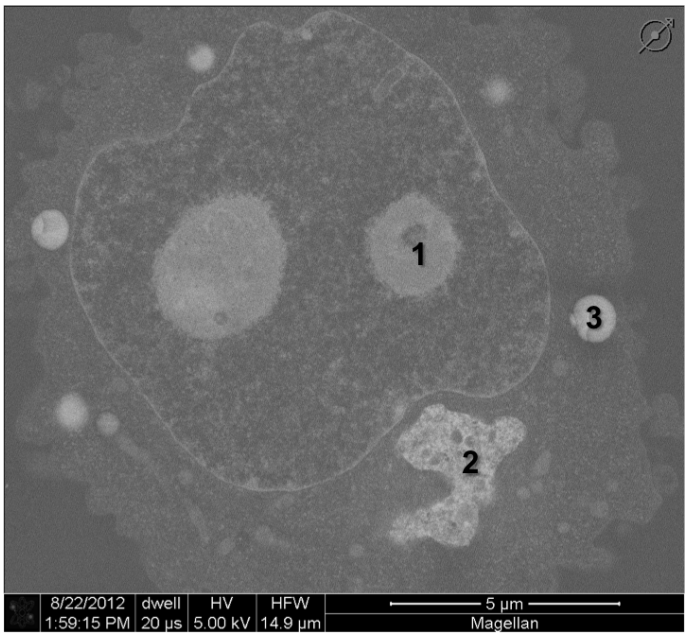

(a)

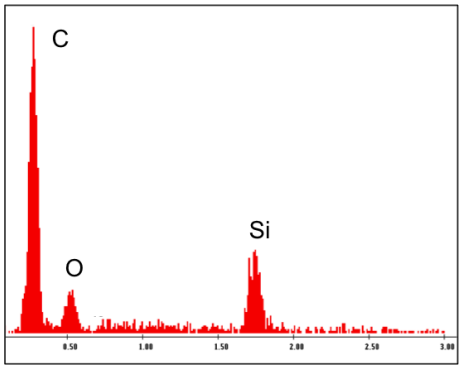

(b)

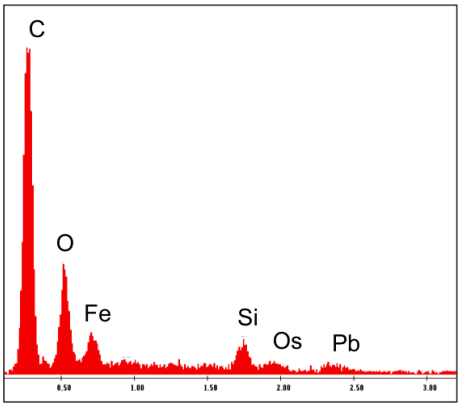

(c)

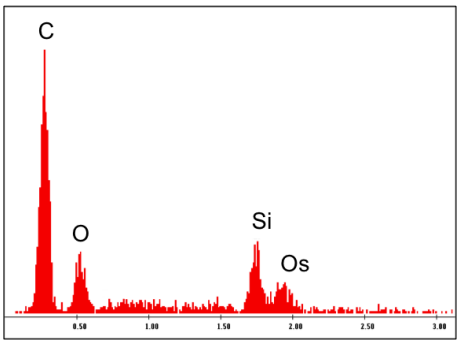

(d)

Figure 3.6: **(a)**SEM of a 400nm thick section of Molday ION labeled 231BR cell. The cell has been stained with osmium and uranyl acetate so that cell structure can be seen. **(b), (c), (d)** correspond to the EDS spectra taken at locations 1, 2, and 3 marked on **(a)**. X-axis is in keV, and notable peaks in the spectra are labeled. **(c)** shows that the SPIO nanoparticles are located in localized packets in various locations of a cell.

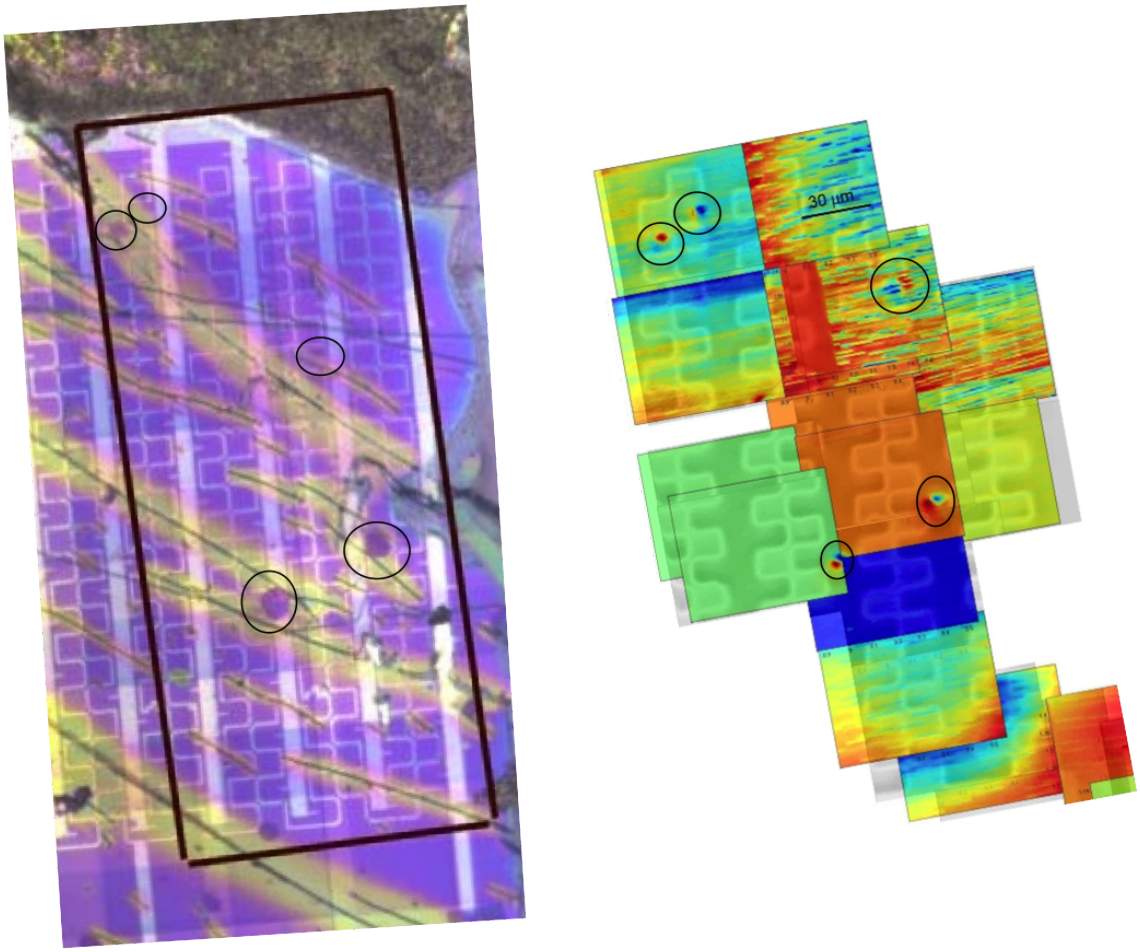

Figure 3.7: Optical image of 400nm sections of SPIO loaded cells (left) and corresponding scanning SQUID magnetometry image (right). The blue tint on the optical image is due to toluidine staining after SQUID images were taken. Grid susceptometry images are overlaid onto the magnetometry image for location identification. The black rectangle on the optical image outlines the scan area of the magnetometry image. Matching cells and dipoles are circled.

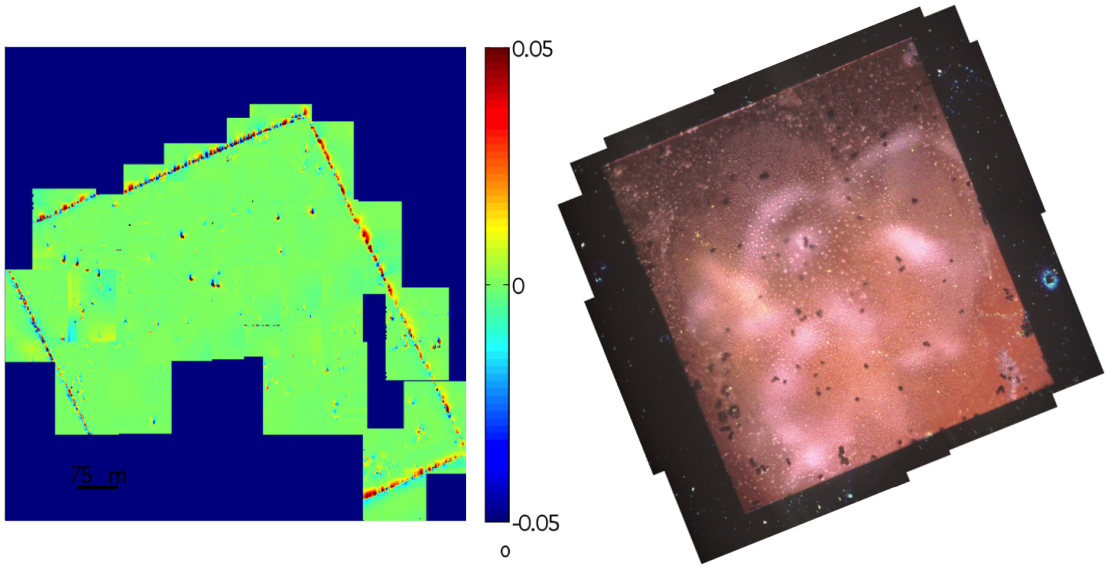

Figure 3.8: Optical image of whole SPIO loaded 231BR cells deposited on a 200nm thin SiN membrane (right) and corresponding magnetometry image (left).

Fig. 3.8 shows our first attempt at imaging whole cells by depositing them on a SiN membrane window and then scanning on the backside. For this first attempt, we had not yet incorporated the gold meander onto the window, which made it difficult to compare magnetometry with optical images. Despite this, by comparing optical images before and after scanning SQUID measurements, it seems like several cells have fallen off or moved around on the membrane during the loading and measurement process. Because the SiN windows are flipped over for scanning and the cells are facing down on the sample mount, there is likely not enough surface tension to keep the cells adhered to the membrane. For the next iteration, we are looking into depositing a thin adhesive on the membrane before adding cells. In addition, we plan to cool down the sample in a magnetic field (a few hundred Gauss would suffice) so that each cell is magnetized during scanning. This would allow us to measure the total magnetic dipole moment of an individual cell.

3.4 Conclusions

In this chapter I discussed our efforts to study mammalian cells genetically encoded to uptake iron like magnetotactic bacteria. If successful, this would enable a genetically encoded MRI contrast agent, allowing for better MRI tracking of cancer cells and stem cells, possibly at the individual cell level. However, to date, expression of certain bacterial genes has not been completed successfully. Instead we have so far been working with mammalian cells loaded with SPIO particles. In particular, we have measured the magnetic signals of individual 231BR cells loaded with Bangs Beads or Molday ION particles using the same tools previously used to study magnetotactic bacteria: MPMS for bulk magnetometry, SEM for locating iron oxide particles within cells, and scanning SQUID magnetometry for imaging single cells.

The main challenge working with mammalian cells as opposed to magnetotactic bacteria is the size of the cells. Unlike the bacteria which are only a few hundred microns thick and about a micron long, the 231BR cells are round and 5-30μm in diameter. This means that the cells must be chemically fixed to preserve their internal structure. In order to identify where SPIO particles are located within the cells, we must take thin cross sections of the cells. New techniques are being developed to scan over the cells using scanning SQUID magnetometry. While using commercially available silicon nitride membrane windows is a possible solution, we must also develop methods to better adhere the cells to the membrane.

Chapter 4

Modeling Magnetic Dipoles

The relatively large dimensions of the SQUID pick-up loop makes quantitative analysis difficult. In this chapter, I will demonstrate a method of analyzing magnetometry images of magnetic dipoles. Specifically, we find the monopole image of our magnetic imaging system by imaging vortices in superconductors, and use this to determine the magnetic dipole moment of various nanomagnets. I will compare this method to image deconvolution and show why it is preferable in the application of obtaining dipole moments. Finally I will present a detailed error analysis.

4.1 Introduction

A scanning SQUID magnetometry image is a convolution of the samples local magnetic induction with with the magnetic sensors point spread function (PSF), also called the imaging kernel. The PSF is sensitive to differences in lithographic dimensions between sensors as well as different alignment conditions between experiments, making precise quantitative analysis of magnetometry images difficult. By imaging superconducting vortices, we find the vortex image of the pick-up loop and can use it to deconvolute the magnetic field of the source image.

In the case of isolated magnetic dipoles, we can combine vortex images to fit similarly taken dipole magnetometry images and calculate their magnetic dipole moments. The model we developed uses seven parameters, some of which may be correlated.

We show that some of these relationships are an intrinsic quality of the model and not an artifact of convolution with the PSF. To perform systematic study of this method, we fabricated and measured cobalt nanomagnets. We show that although we can calculate the magnetic moment using this model, we cannot reliably extract the spatial extent of the dipole.

4.2 Artificial magnetic dipoles

In order to quantify the robustness of the dipole fitting model we developed, we fabricated a series of cobalt nanomagnetic dots and bars with different aspect ratios ranging in size from 20nm×100nm to 1μm×2.5μm, all of which are 30nm thick. Two bars of each size were fabricated to point in orthogonal in-plane directions to test how our image kernel changes with in-plane angle. In order to sufficiently isolate the dipoles from each other while at the same time ensuring that they all fit comfortably within our scan range, the dipoles were spaced 50μm apart from each other. For navigation purposes, the nanomagnets were overlaid onto a silicon wafer containing gold meander patterns. Applying current to the meander creates a magnetic signal that allows for easy location, as described in the previous two chapters.

Nanomagnets were pattered with a JEOL JBX 6300 electron beam lithography system and the meander lines were patterned using standard optical lithography techniques. For the magnetic layer, we deposited 10nm Titanium/30nm Cobalt using an electron beam metal evaporator. Under ambient conditions, cobalt films are expected to naturally form a 5nm non-magnetic oxide layer on all sides [35].

To determine the spatial extent and internal magnetic structure of each dipole, we performed magnetic force microscopy on a Veeco Multimode scanning probe microscope, using a two pass Lift Mode to isolate magnetic forces from sample topography. Figure 4.1 shows scanning electron micrographs (SEM) of a representative nanomagnetic bar, along with corresponding MFM and SQUID magnetometry.

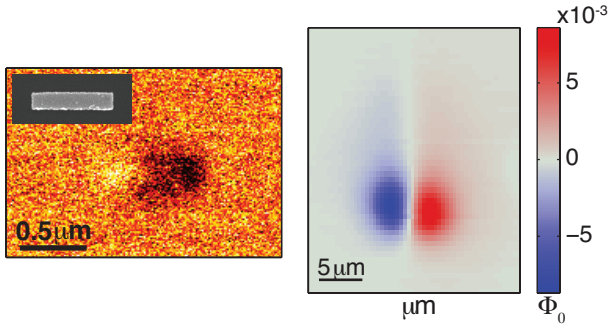

Figure 4.1: Corresponding scanning electron microscopy, magnetic force microscopy and scanning SQUID magnetometry images of a 100nm×600nm×30nm cobalt bar whose moment lies in-plane. A series of these nanomagnets of varying sizes and orientations were fabricated to serve as artificial magnetic dipoles for systematic study of the fitting method.

4.3 Deconvolution

Given a magnetometry image, the most direct way of determining the source image is through image deconvolution. We determined the SQUID point spread function from an experimental flux image of a single crystal of optimally doped $Ba(Fe_{1-x}Co_x)_2As_2$ type II superconductor. Since the estimated penetration depth at low temperatures of this superconductor is about 300nm, ten times smaller than the radius of our pickup loop, we approximate the z-component of the magnetic induction B_z from the vortex to be that of a point monopole:

$$B_z(\vec{r}) = \frac{\Phi_0 z}{2\pi r^2} \tag{4.1}$$

The height of the pickup loop above the sample surface is fixed at z_0. Using the convolution theorem, we take the discrete Fourier transforms $b_z(k_0, k_y, z_0)$ of the monopole magnetic induction $B_z(x, y, z_0)$ and $\phi(k_x, k_y, z_0)$ of the vortex image $\Phi(x, y, z_0)$ to obtain the Fourier transform of the point spread function $p(k_x, k_y)$:

$$p(k_z, k_y) = \frac{\phi(k_x, k_y, z_0)H(k)}{b_z(k_x, k_y, z_0)} \tag{4.2}$$

where the Hanning function $H(k) = (1 + cos(\pi k/k_{max}))/2$ for $k < k_{max}$, 0 otherwise. $k = (k_x^2 + k_y^2)^{1/2}$ and $k_{max} = 2\mu m^{-1}$ cuts off high frequency components. The point spread function $P(x, y)$ is then the inverse Fourier transform of $p(k_x, k_y)$.

A diagram of how the PSF is obtained using a vortex image and calculated magnetic fields from a monopole is shown in Figure 4.2.

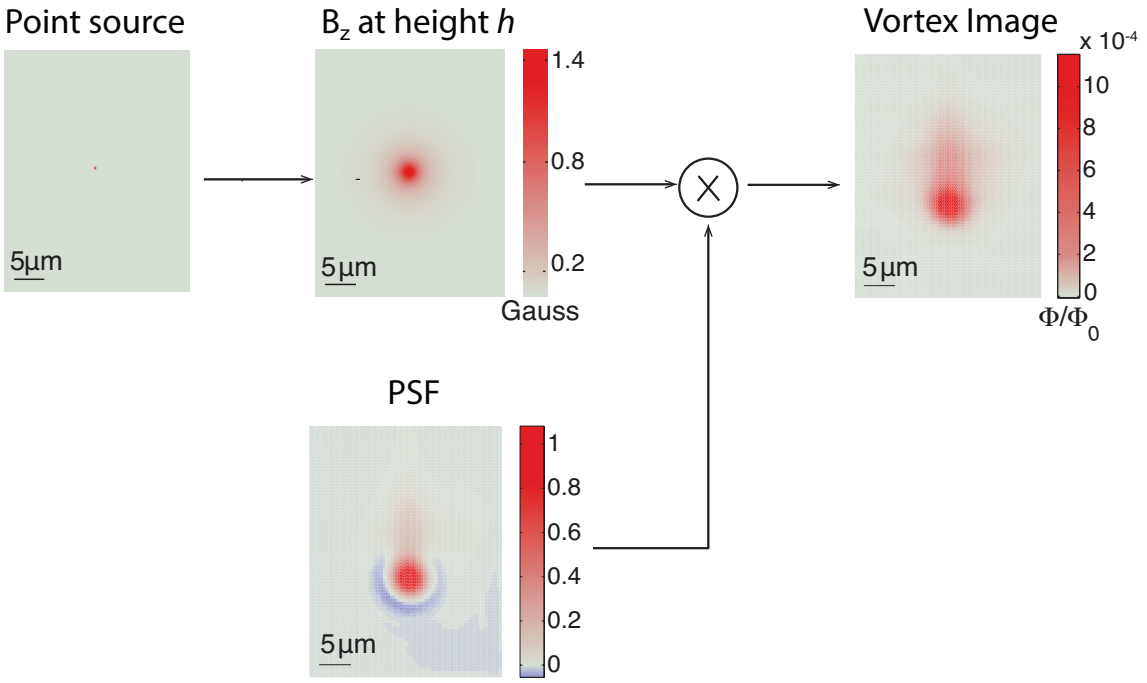

Figure 4.2: Diagram showing how a calculated magnetic point source is propagated to height h and convoluted with the point spread function (PSF) to obtain a SQUID magnetometry image of a superconducting vortex in single crystal $Ba(Fe_{1-x}Co_x)_2As_2$.

A self-consistency check is to calculate the effective pickup area of the sensor:

$$A_{eff} = \iint dxdyP(x, y) = 24.2\mu m^2 \tag{4.3}$$

This is in good agreement with a value of $22\mu m^2$ obtained from measurements of the self-inductance of the SQUID susceptometers used in this paper [21].

We can then use this point spread function to deconvolute the magnetic induction from experimental flux images.

The magnetic flux $\Phi(x, y, z_0)$ is the convolution of $B_z(x, y, z_0)$, the z-component of the magnetic field at the sensor height z_0, with the sensor point spread function $P(x, y)$. Using the deconvolution theorem, the Fourier transform of the field is given by

$$b_z(k_x, k_y, z_0) = \frac{\phi(k_x, k_y, z_0)H(k)}{p(k_x, k_y)} \tag{4.4}$$

where the Hanning function $H(k)$ and the Fourier transform of the point spread function $p(k_x, k_y)$ are as defined above, but in this case we use $K_{max} = 1.5\mu m^{-1}$.

Figure 4.3 depicts this deconvolution process. We see the deconvoluted image is somewhat sharper than the original, and that the most obvious effects of the PSF, the tails to the top of each dipole, have been removed. However, we can also see the effects of the Hanning function in the ring-like ripples that spread out near the centers of the deconvolved dipoles. Because the PSF contains zeros in momentum space, high frequency components must be smoothed out of the Fourier transform of the deconvolved image. For example, for a circular pickup loop with radius a the point spread function in k-space is given by [37]:

$$p(k_x, k_y) = J_1(ka)/(ka/2) \tag{4.5}$$

where J_1 is the first order Bessel function of the first kind. This has a zero at $ka = 3.84$. Therefore Fourier components higher than about $3.84/a$ must be filtered out to avoid numerical instabilities. For source images like magnetic dipoles, which have sharp features, this process may be inaccurate or introduce artifacts. In particular, this filtering leads to an underestimation of the fields from resolution limited dipoles, and therefore an underestimation of their dipole moments.

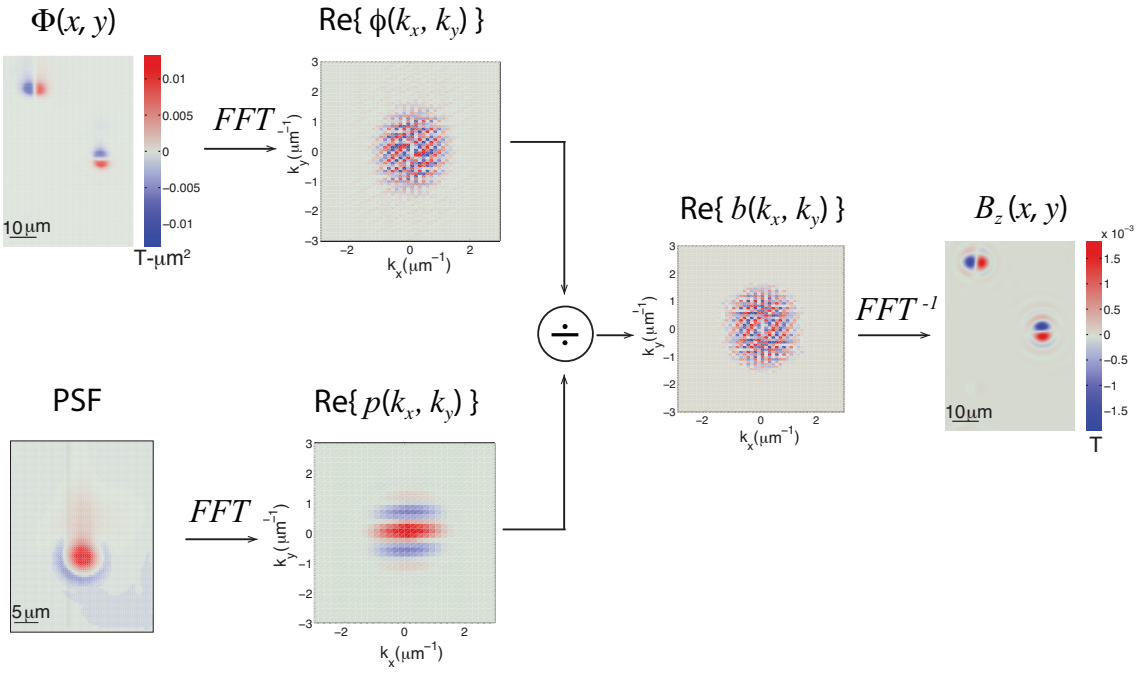

Figure 4.3: Diagram showing how we can use the PSF and the deconvolution theorem to obtain the source magnetic field image $B_z(x, y, h)$ from a SQUID magnetometry image $\Phi(x, y, h)$. A Hanning function with $k_{max} = 1.5\mu m^{-1}$ was applied to cut off high frequency components of $b(k_x, k_y)$. The effects of the Hanning function can be seen by the rings in the deconvoluted image $B_z(x, y, h)$. The SQUID magnetometry image is of two magnetic nanodots 400nm wide and 2500nm long.

4.4 Dipole fitting using vortices

Because of the drawbacks of deconvolution, we present a method of modeling images of magnetic dipoles using images of superconducting vortices and use this model to calculate the magnetic moment of individual dipoles. This method does not require independent knowledge of the PSF and does not require deconvolution.

4.4.1 Description of model and fit parameters

At heights large compared to the penetration depth, the magnetic induction of a superconducting vortex can be described as a magnetic monopole of charge $2\Phi_0/\mu_0$, where $\Phi_0 = h/2e$ is the fundamental flux quantum (Eq. 4.1). To determine the dipole image response, we combine two monopole images. In this work, we focus on the special case of magnetic point dipoles. Just like its electrical analog, we can think of a magnetic dipole as two closely spaced monopoles of equal and opposite charge.

To produce an in-plane dipole, we combine a magnetic monopole of charge $q_v = 2\Phi_0/\mu_0$ with its spatially shifted inverse. The magnetic dipole moment is equal to the spatial separation between the monopoles multiplied by an overall scalar factor, q_m . Shifting in real space is equivalent to multiplication by a phase shift in Fourier space, so this can be written as

$$\vec{B}_{dip}(x,y) = q_m F^{-1}\Big\{e^{-i(k_x x_0 + k_y y_0)}\Big[F\{\bullet\}e^{-\frac{i}{2}(k_x dx + k_y dy)} - F\{\bullet\}e^{\frac{i}{2}(k_x dx + k_y dy)}\Big]\Big\} \quad (4.6)$$

Here, $F\{\bullet\}$ refers to the two-dimensional Fourier transform of the vortex image, where x_0 and y_0 are the coordinates for the center of the dipole, the monopoles are separated in x and y by dx and dy, and k_x and k_y are the two dimensional wave vectors that make up the Fourier space.

To account for the fact that the dipole and vortex images may not be taken at the same height and to allow for out of plane dipole angles, we use the following method to find the field propagation in the z direction. If only vacuum separates the sample

from the imaging plane, the Fourier components of the magnetic field in the imaging plane $z = h$ will be attenuated according to [22]:

$$\vec{b}_k(k_x, k_y, z = h) = \vec{b}_k(k_x, k_y, z = 0)e^{-kh}, h > 0 \tag{4.7}$$

where $k = \sqrt{k_x^2 + k_y^2}$.

Then, for an arbitrarily shaped magnetic field profile $B(x, y, z = h)$, each component of $B(z)$ will be attenuated accordingly:

$$b_k(h) = \sum_{\vec{n}} b_{0,\vec{n}} e^{-kh} e^{-2\pi i \vec{k}\cdot(\frac{\vec{n}}{N})} \tag{4.8}$$

where $\vec{n} = (n_x, n_y)$ is the two-dimensional position vector of each pixel and N is the total number of pixels in the image.

Thus for a SQUID magnetometry image of a vortex, we arrive at the following expression for the dipole image formed by combining the vortex with its inverse extrapolated to $z = z_0, \geq 0$:

$$\vec{B}_{dip}(x, y) = q_m F^{-1}\Big\{e^{kz_0}e^{-i(k_x x_0 + k_y y_0)}\Big[F\{\bullet\}e^{-kdz/2}e^{-\frac{i}{2}(k_x dx + k_y dy)} - F\{\bullet\}e^{kdz/2}e^{\frac{i}{2}(k_x dx + k_y dy)}\Big]\Big\} \tag{4.9}$$

Here, $s_0 = (x_0, y_0, z_0)$ is the center of the dipole with respect to the vortex image, $(dx, dy, dz) = ds$ is the separation between the vortex and its inverse that corresponds to the length of the dipole chain, and q_m is an overall scaling factor that corresponds to the monopole charge. The dipole moment, m, can be calculated as the product of the monopole charge times the separation:

$$m = q_m q_v |ds| \tag{4.10}$$

where $q_v = 2\Phi_0/\mu_0$.

We can fit the data to this model using a trust-region method nonlinear least

squares fitting routine that looks for a χ^2 minimum. The fit uses seven parameters: the monopole charge (q_m), vortex-inverse vortex separation (ds), offset height (z_0), inclination angle (ϕ), azimuthal angle (θ), and the dipole center with respect to the vortex (x_0, y_0).

Figure 4.4a demonstrates how we use the vortex image to fit to the dipole image of the 100nm× 600nm cobalt nanobar shown in Figure 4.1. The residual (data minus fit) of the fit is shown in Figure 4.4b, with a colorbar spanning 10% that of the data. A schematic of the fit parameters is given in Figure 4.4c.

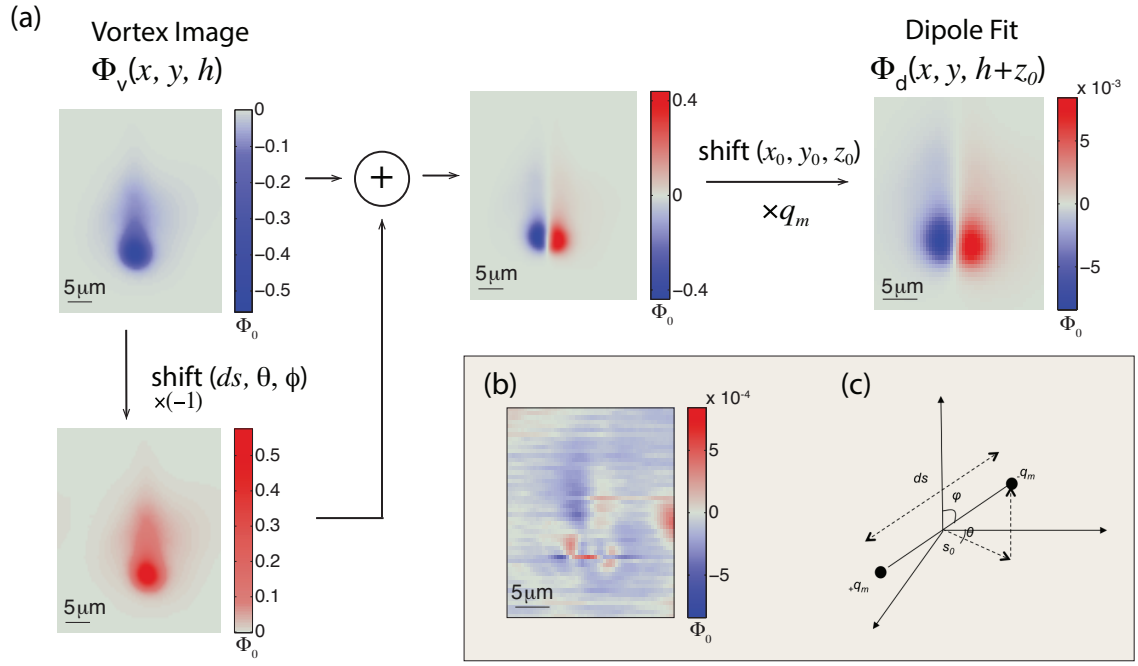

Figure 4.4: **(a)** Diagram of our dipole fitting routine. We use a magnetometry image of a superconducting vortex $\Phi_v(x, y, h)$ to fit a magnetometry image of a dipole $\Phi(x, y, h)$ that may not be taken at the same scan height as the vortex. The dipole fit shown is the best fit for the magnetometry image of the 600nm×100nm nanodot shown in Figure 4.1. **(b)** The residual of the fit shown on a colorscale that covers 0.10 of the scale of the data. **(c)** A schematic of the model and the seven fit parameters used in the fit.

4.4.2 Model conditions and limitations

To reduce systematic errors caused by changes in scanner calibration between cooldowns, deviations in the SQUID image kernel due to lithographic inconsistencies, and variations in SQUID alignment, we measured dipoles and vortices in the same cool down using the same SQUID. We mounted the superconductor and nanomagnet sample substrates by eye to within two degrees in order to minimize systematic errors from differences in SQUID-sample alignment between the vortices and the dipoles.

We note that although the model fits the data quite well, the residuals contain structure (Figure 4.4b). This indicates that the model does not perfectly describe the data. Indeed, this simple model does not take into account the physical size of the magnetic source or any magnetic domain structure. This method limits us to magnetic sources that are small in comparison to the pickup loop (3μm) and scan height (usually 0.5-2μm), where we can approximate the source as a single point dipole.

4.5 Results

4.5.1 Spatial extent of dipole

The point dipole moment is proportional to the product of q_m and ds. We expect these two parameters to be completely correlated if our point dipole approximation is valid. To test if this is the case, we held ds and q_m constant at various values, repeated the fit allowing the other five parameters to vary, and plotted the resulting χ^2 value for each pair (q_m, ds).

Fig. 4.5 shows such plots for two patterned nanomagnets of different lengths (500nm and 900nm), along with their corresponding SEM and MFM images (b, e) and SQUID magnetometry images (c, f). Fig. 4.5a shows that the magnetometry image for the 100nm×500nm nanomagnet behaves like a point dipole. With the q_m and ds axes scaled logarithmically, there is line of near constant minimum χ^2. Although the true global minimum is at $ds \to 0$, χ^2 increases by less than 0.1% of its minimum value along this line for $0.01\mu m < ds < 1\mu m$. Thus, for $ds < 1\mu m$, q_m and ds are

nearly completely correlated, and the fit is only sensitive to the dipole moment, or the product of the two parameters.

Fig. 4.5d shows a similar plot for the 900nm long nanomagnet where we once again have a line of constant χ^2, except this time there is a global minimum at the nonzero $ds = 1.28\mu m$. The value χ^2 representing the point dipole limit is 68% higher than this global minimum. If we set ds to an arbitrarily small value (0.1nm), rather than let it vary, the resulting m is larger by 13% ($1.27 \times 10^8 \mu_B$ versus $1.13 \times 10^8 \mu_B$).

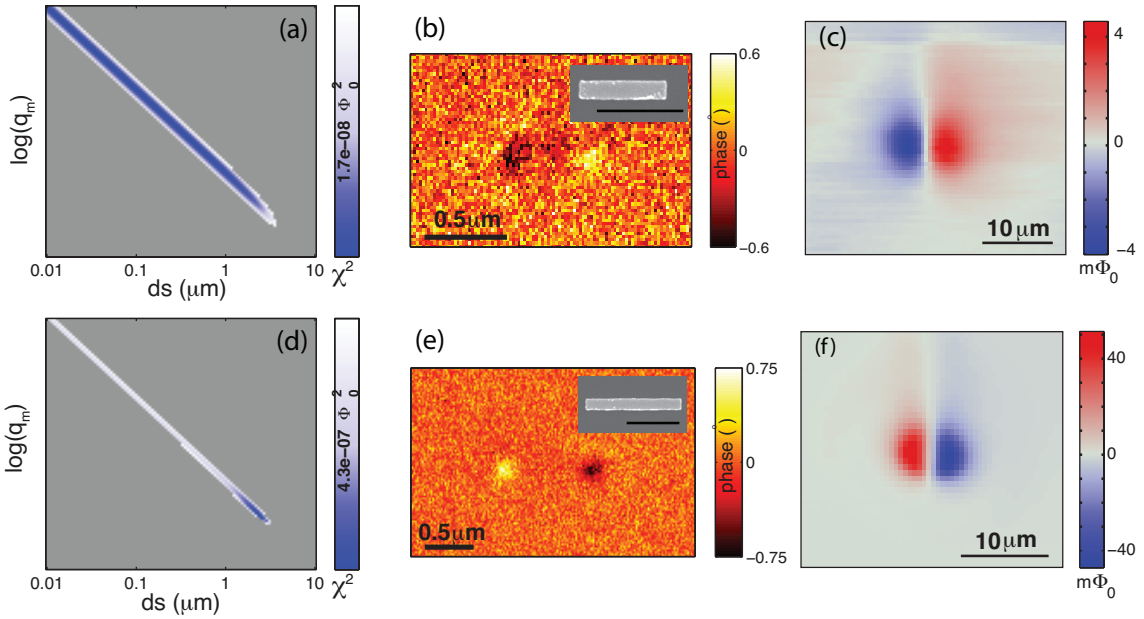

Figure 4.5: Testing for correlation between qm and ds for two dipoles of different physical length. **(a) - (c)** correspond to 100nm×500nm bar, **(d) - (f)** correspond to a 100nm×900nm bar. Scale bar on SEM insets are 500nm. Contours shown in **(a)** and **(c)** are plotted by keeping ds and q_m constant at various values and allowing the other five parameters to vary to minimize χ^2 for each pair (q_m, ds). Grey represents values of $\chi^2 > 2 * min(\chi^2)$. Both dipoles show a line of minimum χ^2 for ds below 1μm, indicating complete correlation between $|ds|$ and q_m. However the 100×900nm dot shows a global minimum at $ds = 1.28\mu m$, which indicates that the fit may give an indication of the physical extent for some dipoles.

Because the fitted value of ds in Fig. 4.5c is close to the physical length of the bar (900nm), we explored the possibility that the fit could provide information on

the spatial extent of the dipole, even for length scales smaller than the pick-up loop size. To this end, we studied the entire row of nanomagnetic bars 100nm wide with lengths ranging from 100nm to 2.5μm. Each magnetometry image was cropped from a larger area scan, with the crop window chosen by visual inspection to contain as much of the dipole as possible without interference from neighboring dipoles. Fitting to these cropped images, we find that in general, the value of ds does not correspond to the physical length of the bar. However, ds is dependent from the crop window chosen, the number of pixels in the scan as well as scan height. Higher pixel count and smaller crop window correspond to larger values of ds, and higher scan heights result in larger ds. Of the magnetometry images from this row that resulted in $ds > 0$, the point dipole limit represented an average of a 37% increase in χ^2 from the fits global minimum. The corresponding increase in fitted moment, m, is on average 12%.

The 7-parameter fit in which we allow ds to vary has the potential to provide information about the spatial extent of a dipole, but this value is too correlated to other scan parameters to be quantitatively useful. For the dipoles that we studied, the fit is not compromised if we approximate the dipole to be a point dipole of infinitesimal ds. For the rest of this paper, we fix $ds = 0.1$nm and fit directly to the dipole moment, thus reducing the number of fit parameters to six. We include the corresponding difference in m as a systematic error.

4.5.2 Error analysis

To obtain the statistical uncertainties of the fitted magnetic moment, we bootstrapped the residuals of the fit [12]. Because our simple point dipole model does not perfectly describe the physical nanomagnets we image, there is some structure in the residuals and this bootstrapping method provides an upper bound on the statistical errors of the fit.

To obtain a lower bound for the systematic errors of the fit for each dipole, we considered the effects of the finite extent of the dipole, incorrect background subtraction, and misalignment between vortex and dipole.

As mentioned in the previous section, in the point dipole approximation, we set

ds to a small number (0.1nm) and fit directly to m. To put a lower bound on the errors of this approximation we repeated the fit by allowing ds to vary and compared the moment to its value at $ds = 0.1$nm. Since we are not including the effects of domain structure in the source dipole, this approach most likely underestimates the errors due to the finite extent of the dipole.

We remove background field gradients due to neighboring dipoles or other magnetic signals by fitting a plane to the perimeter and subtracting it from the magnetometry image. However, because magnetic fields are long range, a smaller crop window means we are leaving out more of the dipolar fields of interest and including them in the background plane that we subtract. A larger crop window means we could be including signals from neighboring sources, and our method of background subtraction may be inadequate. In practice, we choose the crop window for each dipole by eye so that we include as much of the dipole as possible while excluding neighboring dipolar fields. We approximate the error induced in the calculated moment due to background subtraction by varying the crop window within a reasonable range and recording the deviation in m.

Finally we considered the effect of misalignment between vortex and dipole. The two samples are mounted by hand onto the scanning system, and from optical photographs we estimate a misalignment of at most 4°. To calculate how much of an effect this has on the moment, we refitted a dipole with a numerically tilted vortex. We found that a $\pm 2°$ misalignment would cause a 5% change in m.

Fig. 4.6a shows the calculated dipole moment as a function of bar length for the row of 100nm wide cobalt nanomagnets, where x and y bars correspond to the two orthogonal sets of nanomagnets. Thick error bars correspond to the 95% confidence levels each fit calculated by 200 bootstraps. The thin lines correspond to systematic errors, estimated according to the previous paragraphs, added together. The dashed line describes the theoretical relationship between moment and length assuming a 5nm oxidation layer on exposed surfaces and uniform magnetization throughout the rest of the structure with the moment density of bulk cobalt (1422 emu/cm^3). Our data falls slightly below this theoretical line. This is not too surprising, as the 5nm oxidation layer is a lower bound and can vary depending on deposition conditions

and storage conditions. In addition, the nanomagnets are likely broken into domains along their lengths, which will decrease their overall magnetic moments.

Fig. 4.6b shows the fitted moment and corresponding error bars for a 100nm×600nm nanomagnet taken at various scan heights. Again, the error bars are comprised of statistical uncertainties (thicker lines) and systematic uncertainties (thinner lines). Larger scanner voltage (V_z) corresponds to smaller distance between pick-up loop and dipole sample (hence smaller z_0) and is plotted to the left side of the x-axis. From capacitance measurements, we can determine that the SQUID cantilever is in contact with the sample surface at $V_z = 0.8$V. We estimate that this height series covers a z-range of approximately 4μm. All magnetometry images in this height series were cropped to the same dimension, which explains why the systematic uncertainties increase with increasing scan height. At higher heights, the dipolar fields are more spread out, so improper background subtraction contributes more significantly to errors.

However, the three sources of systematic error that we have considered in the preceding paragraphs do not account for 20% decrease in m as the height is increased by 4μm through this height series. This suggests that m and z_0 are correlated parameters, and that allowing z_0 to vary contributes significantly to the systematic errors of the model.

4.5.3 Correlations between parameters

To assess the correlation between m and each of the other five parameters, $p_i (i = 1, 2, 3, 4, 5)$, we plotted the contours for the variation of χ^2 as a function of m and p_i from the least squares fit. Fig. 4.7a-e plots χ^2 as functions of each pair (m, p_i), calculated by holding the other parameters $p_j (j \neq i)$ constant at their optimum values while varying m and p_i. In each plot, the solid black contour corresponds to doubling of χ^2. The tilt of each of these contours indicates the degree of correlation of each pair of parameters with each other [7]. We scaled the axes of each plot so that in the absence of correlation the contours are circles.

These plots show that m is strongly correlated to z_0, but hardly at all to any

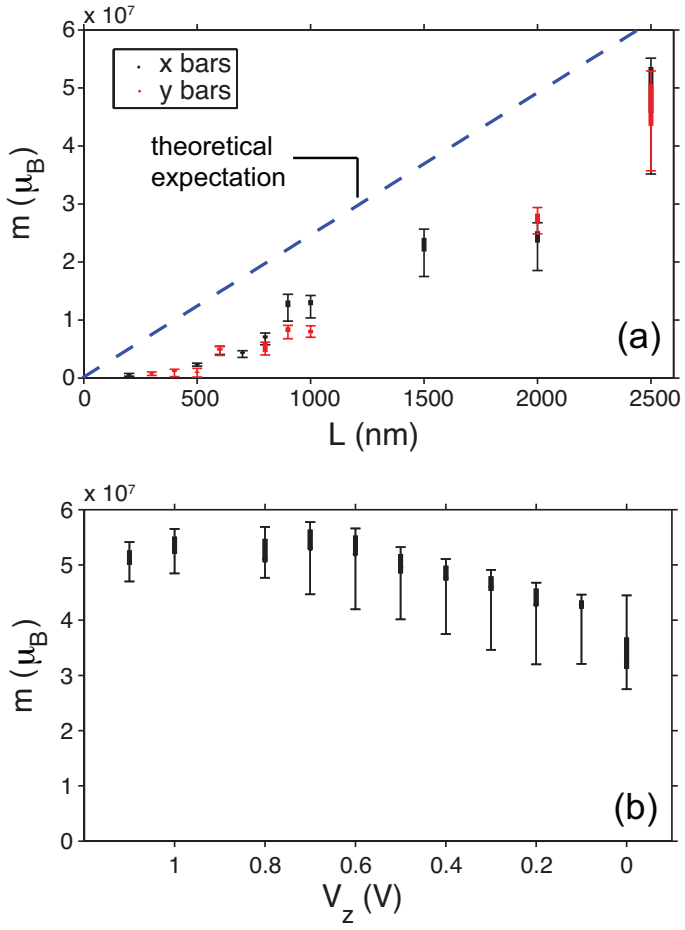

Figure 4.6: **(a)** Fitted dipole moments versus bar length for two sets of cobalt nanomagnets whose moments point in orthogonal directions in plane. All nanomagnets are 30nm thick and 100nm wide. For each point, thicker lines indicate statistical errors calculated by bootstrapping residuals and thinner lines indicate systematic errors calculated according to the text. The dashed blue line indicates the theoretically expected relation between moment and length, assuming a uniform 5nm oxidation layer on exposed surfaces. **(b)** Fitted moment and corresponding error bars for the 100nm×600nm bar taken at various heights. Larger V_z corresponds to smaller distance between pick-up loop and sample. The entire z range covers approximately 4μm. Although the dipole moment should be the same, m decreases with increasing scan height, indicating that uncertainty in z_0 also contributes to systematic errors that are not included in the plotted error bars.

of the other parameters. The correlation between m and z_0 makes sense intuitively because a decrease in magnetometry signal between two dipoles can be attributed to either a increase in scan height or a decrease in dipole moment. The dashed red contour in Fig. 4.7 was calculated by allowing the other four parameters to vary at each pair of values m and z_0 to minimize χ^2. This is equivalent to allowing the other five parameters to assume their best values for each chosen value of m and z_0. This contour is identical to the solid black contour, indicating that there is virtually no correlation between either of these two parameters with the others.

4.6 Simulated Dipoles to Study Model

Our data appears to show that some of the parameters used in our fitting method are linked together in such a way that the fitting algorithm is unable to distinguish between them. In particular, there seems to be a correlation between ds and z_0, as well as between m and z_0. We wish to determine if these relationships are an artifact of convolution with the SQUID kernel or if they are an intrinsic quality of the model. To do this, we remove the SQUID from the picture entirely and perform theoretical calculations using the magnetic field from simulated dipoles.

Consider a classical magnetic dipole made from the superposition of two monopoles of equal and opposite magnetic charge. We can write the field due this dipole as

$$\vec{B}(x,y,z) = \frac{q_m}{r_1^2}\hat{r_1} - \frac{q_m}{r_2^2}\hat{r_2} \tag{4.11}$$

where q_m is the magnetic monopole charge and r_1, r_2 are vectors pointing from particle 1 and particle 2 to the location (x, y, z), respectively. The SQUID pickup loop measures magnetic flux, so we consider only the z component of the magnetic field. Let us assume the simple case of a dipole oriented only along the x-axis. Then the simplified equation for B_z is:

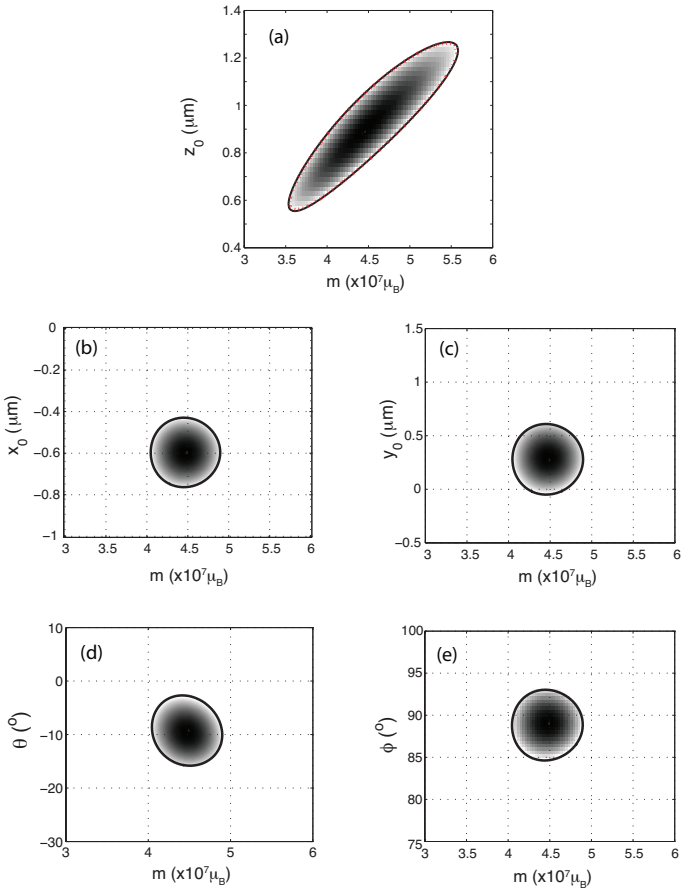

Figure 4.7: **(a)-(e)** χ^2 as functions of m and each of the other parameters, p_i, calculated by holding parameters $p_j (j \neq i)$ constant at their optimum values while varying m and p_i. In each plot, the dashed line in each plot is the contour corresponding to doubling of χ^2 from its minimum value. The tilt of each of these contours indicates the degree of correlation of each pair of parameters with each other. We scaled the vertical axes of each plot so that in the absence of correlation the contours lines are circles. These plots demonstrate that z_0 is strongly correlated to m, while the other parameters are only very weakly correlated to m. In **(a)**, the dashed red contour is calculated by also allowing the other parameters to vary to minimize χ^2 for each pair of values m and z_0. This indicates that while z_0 is correlated to m, it is not correlated to the other parameters.

$$B_z = \frac{q_m z_0}{\left((x - x_0 + ds/2)^2 + (y - y_0)^2 + z_0^2\right)^{3/2}} - \frac{q_m z_0}{\left((x - x_0 - ds/2)^2 + (y - y_0)^2 + z_0^2\right)^{3/2}} \tag{4.12}$$

To determine if there is a correlation between ds and z_0 in the model, we generate data sets using Equation 4.12, apply white Gaussian noise and attempt to fit to the resulting image using Equation 4.12.

We now plot various fitted parameters as a function of the actual height of the simulated dipole scan as follows. ds is kept at a constant value of 0.2μm for all plots. The monopole charge, q_m, is kept at a constant value of $5 \times 10^7 \mu_B/\mu$m, so the dipole moment for each dataset is $1.0 \times 10^7 \mu_B$. z_0 is varied linearly between 0.4μm and 3μm. For each value of z_0, a dipole is produced using Equation 4.12. White Gaussian noise is applied to the image with a signal to noise ration (SNR) of 30 and the parameters are fit the resulting image. We study the fitted values of ds, z_0 and m as a function of the actual height z_0. The process is repeated 100 times to obtain bootstrap estimates of the fit parameters and their statistical errors. The mean of the 100 fits is taken to be the value of the parameter, and the standard deviation is taken to be the uncertainty. We do not perform any background subtraction. Fig. 4.8 shows the results.

In each plot, the solid line corresponds to the true value of each parameter. We see that the fitted value of ds tends to overestimate its true value as z_0 is increased. But the fitted dipole moment m remains constant at its expected value because the fitted value of q_m adjusts to compensate for ds. We see that in the absence of the SQUID kernel and systematic sources of error such as background subtraction and non-ideal magnetic domain structure, m and z_0 are completely separable parameters. In particular, the fitted moment m does not depend on height z_0 for $z_0 \gg ds$. However, the fitted value of ds does depend on z_0, increasing by roughly a factor of two as z_0 is increased from 0.4μm to 3μm. This suggests that the correlation between ds and z_0 is intrinsic to the model and cannot be avoided.

We can show that in the limit of $z_0 \gg ds$, B_z depends only on the magnetic

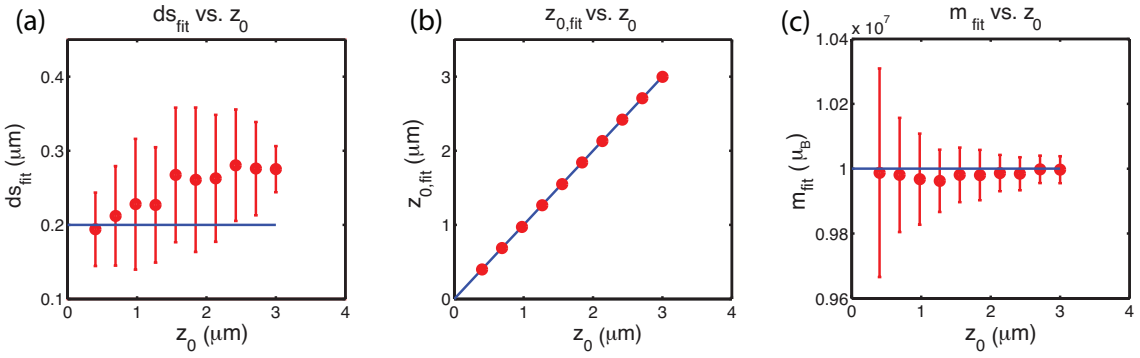

Figure 4.8: Using theoretically calculated magnetic dipole fields to study the dipole fitting scheme without the effects of the SQUID image kernel. All simulated dipoles have Gaussian white noise added so that the SNR is 30. Plots show relationships between fitted **(a)** ds, **(b)** z_0 and **(c)** m on actual height propagation z_0. Error bars are derived from 100 bootstraps, and the solid line indicates the actual value of each parameter. **(b)** and **(c)** show that m is theoretically independent from z_0. The reduction in error at higher heights in **(c)** is most likely due to the inclusion of extra information in the tails of the image for larger z_0. However, **(a)** shows that fitting values of ds contain large statistical error bars and vary with z_0. This indicates that uncertainties in ds are intrinsic to our model and not merely a result of convolution with the SQUID image kernel or experimental sources of systematic uncertainty.

moment rather on q_m and ds separately. Let $z_0 \gg ds$ so that $\epsilon = ds/2h \ll 1$. Then from Equation 4.12 we can write

$$B_z = \frac{q_m}{z_0^2}\left[\frac{1}{\left(1+(y/z_0)^2+(x/z_0+\epsilon)^2\right)^{3/2}} - \frac{1}{\left(1+(y/z_0)^2+(x/z_0-\epsilon)^2\right)^{3/2}}\right] \quad (4.13)$$

Here we have the dipole centered about the origin for simplicity. If we expand B_z in powers of ϵ and disregard higher order terms, we find

$$B_z \approx -\frac{3xz_0m}{(z_0^2+x^2+y^2)^{3/2}} \quad (4.14)$$

4.7 Discussion

In this chapter, I described the modeling technique that was used to calculate the dipole moment from scanning SQUID magnetometry images in Chapter 2 and 3.

I demonstrated how a superconducting vortex can determine the point spread function of a magnetic imaging sensor. This PSF can be used to deconvolute magnetic flux images and infer source magnetic fields from dipoles. However, because the PSF contains zeros, deconvolution is not the ideal way to analyze dipole images. I described a technique to fit to scanning SQUID magnetometry images of point dipoles and calculate the magnetic moment and orientation of each dipole. This technique uses a vortex as the sensors monopole image and does not require determination of the PSF. By studying patterned nanomagnets of various sizes, we conclude that we cannot reliably determine the spatial extent of dipoles for dipole extents much smaller than the pickup loop radius using this model. Theoretical calculations confirm that this is a feature of the model itself and not a effect of the SQUID kernel. Our error analysis shows that this methods uncertainties are dominated by systematic errors, and that in particular, the magnetic moment calculated from this technique is strongly correlated to scan height. Theoretically, the moment and height should be independent in our model, so this correlation is most likely due to effects of background subtraction and/or the SQUID image kernel. We are currently investigating

ways to more accurately determine scan height and hope to eventually remove it as a fitting parameter.

This technique can be used for a variety of scanning magnetic probes, and may also be used to analyze more complicated magnetic configurations.

Chapter 5

Future Directions

In Chapter 1, I introduced applications of iron oxide based nanomagnets for use in biomedicine applications. In particular, I discussed how image contrast is obtained in MRI and how nanomagnets can be used as contrast agents. As many of these applications approach the single cell level, it becomes increasingly important to develop magnetic characterization techniques that are capable of quantitatively measuring magnetic properties of single cells. I introduced potential instruments that possess the spatial resolution and magnetic sensitivity for such a task - in particular, the scanning SQUID microscope. Although our scanning SQUID microscope only operates at cryogenic temperatures and under high vaccuum, the technique has a noise floor of $200\mu_B/\sqrt{Hz}$ and a spatial resolution of under 5μm.

In Chapters 2 and 3, I discussed how we can use the scanning SQUID microscope to measure individual magnetotactic bacteria and SPIO loaded mammalian cells. Coarse scanners allow a maximum range of 5mm×5mm and a gold meander grid allows accurate position location on our sample so that we can match magnetometry signals with optical and/or scanning electron microscopy images of the sample. Analysis of two groups of magnetotactic bacteria that were supplemented different forms of iron showed that more 70% of the cells we studied did not contain iron oxide particles, and amongst those that did, the individual magnetic moments spanned two orders of magnetitude. These insights cannot be obtained from using a bulk magnetometer to study the average magnetic moment of each population.

Finally in Chapter 4, I presented a method of quantitatively analyzing scanning SQUID magnetometry images of individual dipoles which combines two images of monopoles obtained from a superconducting vortex. This fitting technique was compared to image deconvolution. A series of nanomagnets of varying sizes were fabricated to systematically study the fit and quantify error sources.

In this final chapter, I will present future directions for this work.

5.1 Dipole analysis

The greatest source of uncertainty in the dipole fitting technique comes from uncertainty in height, z_0. This uncertainty could be eliminated if the crop window were infinitely large, thus containing all of the magnetic field. Although this is not possible and depends on how closely spaced the cells are, more work should be done to optimize the best crop window for a given dipole given its surroundings and the pixel density of the image. In practice, adjusting the crop window by only one or two pixels on a side can have a noticeable affect on the fitted errors in crowded images. The crop window is related to and affected by background subtraction. Thus effort should be taken to determine how best to perform background subtraction once a crop window has been determined.

The approach used in the work presented in this thesis is to:

1. Manually identify dipole in large area scan and choose a crop window that roughly encompasses as much of the dipole as possible while not enclosing significant signals from surrounding dipole or other magnetic features.

2. Fit a plane to the perimeter of this cropped scan, subtract this plane from the image, then fit the resulting flux image according to the Chapter 4.

3. Adjust the crop window by a few pixels on each side, repeat the above step, and choose the cropped image and fitted values that correspond to the best fit (minimum χ^2 error).

Subtracting a plane is not the ideal background subtraction method because many times the background on which the dipole sits cannot be accurately approximated as

a plane. More importantly, when the crop window is small, the plane defined by the perimeter contains significant portions of the dipole itself and subtracting it will alter the shape and amplitude of the dipole. This distortion is increasingly worse at higher scan heights (assuming that crop window is kept constant) because the dipole becomes more spread out. In other words, much of the height dependence of the calculated moment is due to the background subtraction.

In some large area scans, Gaussian filters can be applied to smooth a bumpy background. However this technique is not appropriate if the background magnetic fields are varying at the same length scales as the dipoles themselves, or if the goal is remove signals from neighboring dipoles. Custom filters should be explored to alleviate this problem.

Another obvious shortcoming of the fitting method described above is the manual process in which dipoles are selected. Since the goal of the scanning SQUID technique is to image tens or hundreds of dipoles in each experiment, manually detecting individual dipoles is very time consuming and not scalable. In addition, because the measured dipoles can span several orders of magnitude in intensity, it is easy to miss weaker dipoles if we are manually selecting dipoles from an image whose colorscale is dominated by stronger dipoles. Automatic dipole detection has been implemented to solve these problems. Both peak-antipeak detection and a machine learning classification algorithm using a sliding window technique have been implemented successfully. In each case, it is still necessary to manually check at the end to filter out false positives or identify clusters that cannot be fitted. In addition, it is still necessary to perform step 3 by hand to determine the best crop window.

A dipole detection algorithm with the ability to determine the appropriate crop window and perform appropriate background subtraction that keeps the structure and intensity of the dipole intact will greatly improve the accuracy and performance of the fitting technique.

5.2 Instrumentation

The most significant disadvantage of using scanning SQUID for biological measurements are the cryogenic operational conditions required. All scanning SQUID measurements described in this thesis were performed at 4K at high vacuum conditions ($< 10^{-6}$torr). Under better vacuum conditions, the sample and SQUID are thermally isolated so the sample can be raised to higher temperatures. However, in the current setup, the sample will still have to be placed under vacuum and first cooled down to 4K. These conditions are completely different from natural conditions in which bacteria or mammalian cells live. Not only is it not possible to image live cells, but it is likely that cell structure and magnetic properties are altered during death. This is less of a problem with the mammalian cells we studied, which had been chemically fixed prior to measuring, thus preserving the cell structure.

An ideal system for measuring magnetic properties of cells would operate at room temperature, with live cells, in conditions similar to those in which they will be used at. Recent work using diamond NV center magnetometry has shown the ability to image live magnetotactic bacteria at room temperature [28]. In this work, the authors used a wide-field fluorescence microscope to obtain combined magnetic and optical images with 400nm resolution. Live bacteria in PBS were placed on the surface of a diamond chip with NV center implants. By exciting the NV centers with a laser beam, the authors were able to obtain large area vector magnetic field images and correlate them to bright field optical images using the same instrument. Using this technique, one can measure many individual bacteria in one experiment, similar to what we did using scanning SQUID magnetometry, obtain population statistics. However, quantitative analysis is non-trivial, as the technique measures the magnetic field vector and not the dipole moment directly.

Bibliography

[1] R Allenspach. Spin-polarized scanning electron microscopy. *Journal of electron microscopy*, 62(1):177–91, January 2013.

[2] DA Allwood, Gang Xiong, MD Cooke, and RP Cowburn. Magneto-optical Kerr effect analysis of magnetic nanostructures. *Journal of Physics D: Applied Physics*, 2175, 2003.

[3] E. Amaladass, B. Ludescher, G. Schutz, T. Tyliszczak, and T. Eimuller. Size dependence in the magnetization reversal of FeGd multilayers on self-assembled arrays of nanospheres. *Applied Physics Letters*, 91(17):172514, 2007.

[4] Leisha M. Armijo, Yekaterina I. Brandt, Dimple Mathew, Surabhi Yadav, Salomon Maestas, Antonio C. Rivera, Nathaniel C. Cook, Nathan J. Withers, Gennady a. Smolyakov, Natalie L. Adolphi, Todd C. Monson, Dale L. Huber, Hugh D. C. Smyth, and Marek Osiski. Iron Oxide Nanocrystals for Magnetic Hyperthermia Applications. *Nanomaterials*, 2(4):134–146, May 2012.

[5] Dennis a Bazylinski. Controlled biomineratlization of magnetic minerals by magnetotactic bacteria. *Chemical Geology*, 132:191–198, 1996.

[6] Michael R Benoit, Dirk Mayer, Yoram Barak, Ian Y Chen, Wei Hu, Zhen Cheng, Shan X Wang, Daniel M Spielman, Sanjiv S Gambhir, and a Matin. Visualizing implanted tumors in mice with magnetic resonance imaging using magnetotactic bacteria. *Clinical cancer research : an official journal of the American Association for Cancer Research*, 15(16):5170–7, August 2009.

[7] Philip Bevington and D. Keith Robinson. *Data Reduction and Error Analysis for the Physical Sciences*. McGraw-Hill Science/Engineering/Math, 3 edition, 2002.

[8] Richard Blakemore. Magnetotactic Bacteria. *Science*, 190(4212):377–379, 1975.

[9] Zhifeng Deng, Erhan Yenilmez, Josh Leu, J. E. Hoffman, Eric W. J. Straver, Hongjie Dai, and Kathryn a. Moler. Metal-coated carbon nanotube tips for magnetic force microscopy. *Applied Physics Letters*, 85(25):6263, 2004.

[10] R. E. Dunin-Borkowski. Magnetic Microstructure of Magnetotactic Bacteria by Electron Holography. *Science*, 282(5395):1868–1870, December 1998.

[11] Rafal E Dunin-Borkowski, T Kasama, and RJ Harrison. Electron Holography of Nanostructured Materials. In Angus I Kirkland and John L. Hutchison, editors, *Nanocharacterisation*, chapter 5, pages 138–162. Royal Society of Chemistry, 2007.

[12] Bradley Efron and Robert J Tibshirani. *An Introduction to the Bootstrap*. Chapman & Hall/CRC, 1 edition, 1994.

[13] M Luisa Fdez-Gubieda, Alicia Muela, Javier Alonso, Ana Garcia-Prieto, Luca Olivi, Rodrigo Fernandez-Pacheco, and Jose Manuel Barandiara. Magnetite Biomineralization in Magnetospirillum gryphiswaldense : Time-Resolved Magnetic and Structural Studies. *ACS Nano*, 2013.

[14] Richard B. Frankel and Dennis a. Bazylinski. Magnetotaxis and magnetic particles in bacteria. *Hyperfine Interactions*, 90(1):135–142, December 1994.

[15] Islam Hamad, Othman Al-hanbali, A Christy Hunter, Kenneth J Rutt, Thomas L Andresen, and S Moein Moghimi. Switching of Complement Activation Pathways at the Nanosphere Serum Interface : Implications for Stealth Nanoparticle Engineering. *ACS Nano*, 4(11):6629–6638, 2010.

[16] Chris Heyn, Chris V Bowen, Brian K Rutt, and Paula J Foster. Detection threshold of single SPIO-labeled cells with FIESTA. *Magnetic resonance in*

medicine : official journal of the Society of Magnetic Resonance in Medicine / Society of Magnetic Resonance in Medicine, 53(2):312–20, February 2005.

[17] Chris Heyn, John a Ronald, Lisa T Mackenzie, Ian C MacDonald, Ann F Chambers, Brian K Rutt, and Paula J Foster. In vivo magnetic resonance imaging of single cells in mouse brain with optical validation. *Magnetic resonance in medicine : official journal of the Society of Magnetic Resonance in Medicine / Society of Magnetic Resonance in Medicine*, 55(1):23–9, January 2006.

[18] Martin E Huber, Nicholas C Koshnick, Hendrik Bluhm, Leonard J Archuleta, Tommy Azua, Per G Björnsson, Brian W Gardner, Sean T Halloran, Erik a Lucero, and Kathryn a Moler. Gradiometric micro-SQUID susceptometer for scanning measurements of mesoscopic samples. *The Review of scientific instruments*, 79(5):053704, May 2008.

[19] Akira Ito, Hirokazu Akiyama, Yoshinori Kawabe, and Masamichi Kamihira. Magnetic force-based cell patterning using Arg-Gly-Asp (RGD) peptide-conjugated magnetite cationic liposomes. *Journal of bioscience and bioengineering*, 104(4):288–93, October 2007.

[20] Tapan K Jain, John Richey, Michelle Strand, Diandra L Leslie-Pelecky, Chris a Flask, and Vinod Labhasetwar. Magnetic nanoparticles with dual functional properties: drug delivery and magnetic resonance imaging. *Biomaterials*, 29(29):4012–21, October 2008.

[21] J. Kirtley, B. Kalisky, J. Bert, C. Bell, M. Kim, Y. Hikita, H. Hwang, J. Ngai, Y. Segal, F. Walker, C. Ahn, and K. Moler. Scanning SQUID susceptometry of a paramagnetic superconductor. *Physical Review B*, 85(22), June 2012.

[22] V. Kogan. Meissner response of anisotropic superconductors. *Physical Review B*, 68(10):1–7, September 2003.

[23] Nicholas C. Koshnick, Martin E. Huber, Julie A. Bert, Clifford W. Hicks, Jeff

Large, Hal Edwards, and Kathryn A. Moler. A terraced scanning superconducting quantum interference device susceptometer with submicron pickup loops. *Applied Physics Letters*, 93(24):243101, January 2008.

[24] H Kuramochi, T Uzumaki, M Yasutake, a Tanaka, H Akinaga, and H Yokoyama. A magnetic force microscope using CoFe-coated carbon nanotube probes. *Nanotechnology*, 16(1):24–27, January 2005.

[25] L.-M. Lacroix, R. Bel Malaki, J. Carrey, S. Lachaize, M. Respaud, G. F. Goya, and B. Chaudret. Magnetic hyperthermia in single-domain monodisperse FeCo nanoparticles: Evidences for StonerWohlfarth behavior and large losses. *Journal of Applied Physics*, 105(2):023911, 2009.

[26] Kevin J Landmark, Stassi Dimaggio, Jesse Ward, Christopher Kelly, Stefan Vogt, Seungpyo Hong, Alina Kotlyar, Andrzej Myc, Thommey P Thomas, James E Penner-hahn, James R Baker, Mark M Banaszak Holl, and Bradford G Orr. Testing of Superparamagnetic Iron Oxide Nanoparticles Targeted Using Folic Acid-Conjugated Dendrimers. *ACS Nano*, 2(4):773–783, 2008.

[27] Robert Langer and Joseph P Vacanti. Tissue Engineering. *Science*, 260:920–926, 1993.

[28] D Le Sage, K Arai, D R Glenn, S J DeVience, L M Pham, L Rahn-Lee, M D Lukin, a Yacoby, a Komeili, and R L Walsworth. Optical magnetic imaging of living cells. *Nature*, 496(7446):486–9, April 2013.

[29] Sarah R MacEwan, Daniel J Callahan, and Ashutosh Chilkoti. Stimulus-responsive macromolecules and nanoparticles for cancer drug delivery. *Nanomedicine (London, England)*, 5(5):793–806, July 2010.

[30] Martha R. McCartney and David J. Smith. Electron Holography: Phase Imaging with Nanometer Resolution. *Annual Review of Materials Research*, 37(1):729–767, August 2007.

[31] Meng Meng Lin, Hyung-Hwan Kim, Hyuck Kim, Mamoun Muhammed, and Do Kyung Kim. Iron oxide-based nanomagnets in nanomedicine: fabrication and applications. *Nano reviews*, 1:1–17, January 2010.

[32] Paul a Midgley and Rafal E Dunin-Borkowski. Electron tomography and holography in materials science. *Nature materials*, 8(4):271–80, April 2009.

[33] R B Proksch, T E Scha, B M Moskowitz, E D Dahlberg, D A Bazylinski, and R B Frankel. Magnetic force microscopy of the submicron magnetic assembly in a magnetotactic bacterium . *Applied Physics Letters*, 66(19):2582–2584, 1995.

[34] Quantum Design Inc. http://www.qdusa.com/products/mpms-squid-vsm.html.

[35] B. Rellinghaus, S. Fernandez DeAvila, G. Armelles, R. Beyers, a. Kellock, and D. Weller. Natural oxide formation on cobalt investigated with the magneto-optical Kerr effect. *IEEE Transactions on Magnetics*, 33(5):3238–3240, 1997.

[36] a Fraile Rodríguez, a Kleibert, J Bansmann, and F Nolting. Probing single magnetic nanoparticles by polarization-dependent soft x-ray absorption spectromicroscopy. *Journal of Physics D: Applied Physics*, 43(47):474006, December 2010.

[37] Bradley J. Roth, Nestor G. Sepulveda, and John P. Wikswo. Using a magnetometer to image a two-dimensional current distribution. *Journal of Applied Physics*, 65(1):361, January 1989.

[38] Zm Saiyed, Sd Telang, and Cn Ramchand. Application of magnetic techniques in the field of drug discovery and biomedicine. *Biomagnetic research and technology*, 1(1):2, September 2003.

[39] F Scherer, M Anton, U Schillinger, J Henke, C Bergemann, A Krüger, B Gänsbacher, and C Plank. Magnetofection: enhancing and targeting gene delivery by magnetic force in vitro and in vivo. *Gene Therapy*, 9(2):102–109, 2002.

[40] G Schutz, W Wagner, W Wilhelm, P Kienle, R Zeller, R Frahm, and G Materlik. Absorption of CIrcularly Polarized X Rays in Iron. *Physical Review Letters*, 58(7):737–740, 1987.

[41] David Serrate, Paolo Ferriani, Yasuo Yoshida, Saw-Wai Hla, Matthias Menzel, Kirsten von Bergmann, Stefan Heinze, Andre Kubetzka, and Roland Wiesendanger. Imaging and manipulating the spin direction of individual atoms. *Nature nanotechnology*, 5(5):350–3, May 2010.

[42] Robert B Sim and Russell Wallis. Surface properties: Immune attack on nanoparticles. *Nature nanotechnology*, 6(2):80–1, February 2011.

[43] Andreas Winkler, Thomas Muhl, Siegfried Menzel, Radinka Kozhuharova-Koseva, Silke Hampel, Albrecht Leonhardt, and Bernd Buchner. Magnetic force microscopy sensors using iron-filled carbon nanotubes. *Journal of Applied Physics*, 99(10):104905, 2006.

[44] J. Wu, D. S. Schmool, N. D. Hughes, J. R. Moore, and R. J. Hicken. Picosecond large angle reorientation of the magnetization in Ni[sub 81]Fe[sub 19] circular thin-film elements. *Journal of Applied Physics*, 91(1):278, 2002.

[45] Jing Xia, Peter T. Beyersdorf, M. M. Fejer, and Aharon Kapitulnik. Modified Sagnac interferometer for high-sensitivity magneto-optic measurements at cryogenic temperatures. *Applied Physics Letters*, 89(6):062508, 2006.

[46] G. Yang, J. Tang, S. Kato, Q. Zhang, L. C. Qin, M. Woodson, J. Liu, J. W. Kim, P. T. Littlehei, C. Park, and O. Zhou. Magnetic nanowire based high resolution magnetic force microscope probes. *Applied Physics Letters*, 87(12):123507, 2005.

[47] Omar Zurkiya, Anthony W S Chan, and Xiaoping Hu. MagA is sufficient for producing magnetic nanoparticles in mammalian cells, making it an MRI reporter. *Magnetic resonance in medicine : official journal of the Society of Magnetic Resonance in Medicine / Society of Magnetic Resonance in Medicine*, 59(6):1225–31, June 2008.

Lisa Qian

I certify that I have read this dissertation and that, in my opinion, it is fully adequate in scope and quality as a dissertation for the degree of Doctor of Philosophy.

(Kathryn Moler) Principal Advisor

I certify that I have read this dissertation and that, in my opinion, it is fully adequate in scope and quality as a dissertation for the degree of Doctor of Philosophy.

(Ian Fisher)

I certify that I have read this dissertation and that, in my opinion, it is fully adequate in scope and quality as a dissertation for the degree of Doctor of Philosophy.

(Malcolm Beasley)

Approved for the University Committee on Graduate Studies